

# Entropy-Patch Choked-Nozzle Interaction: Inertial, quasi-steady, linear, and non-linear modeling regimes mapped

Master Thesis

**Author:** Karim Elbakly

**Committee Members:**

Prof. dr. ir. C.H. Venner (chair)

Dr. ir. L. Hirschberg (supervisor)

Dr. ir. Y.H. Wijnant (internal member)

Dr. M. Mehrali (internal member)

Dr. S.J. Hulshoff (external member)

Dr. A. Genot (external member)

**Document Number:** EFD-470

June, 2025

Engineering Fluid Dynamics Group,  
Faculty of Engineering Technology,  
University of Twente

# Preface

This thesis marks the end of my Master's journey, yet signifies a new beginning as I continue along the path of academic exploration. It represents the culmination of a period filled with challenging yet rewarding times of exploring the unknowns, personal growth, and renewed interests.

Throughout this process, I have been fortunate to receive support and guidance from many individuals. I would like to express my sincere gratitude to my supervisor, Dr. Lionel Hirschberg, whose insights, encouragement, and patience were crucial to the completion of this work. Beyond his academic support, I am especially thankful for the friendship that developed along the way.

I am also especially grateful to Prof. Kees Venner, whose support made it possible for me to present my work at the 17e Congrès Français d'Acoustique and the 2025 Burgers Symposium. These opportunities not only enriched my academic experience but also deepened my confidence and enthusiasm for contributing to the field.

A special thanks goes to Dr. Steven Hulshoff, Prof. Avraham Hirschberg, and Dr. Marijn Sanders, whose encouragement and advice made this journey not only more manageable, but also far more enjoyable.

Last but not least, this thesis would not have been possible without the unwavering support of my family and friends, who stood by me through every stage. Their belief in me has been a constant source of strength.

As I reflect on the experiences behind this thesis, I do so with gratitude for the knowledge gained, the relationships built, the challenges overcome, and the opportunities that lie ahead.

And always remember, "Thinking about thinking is the hardest type of thinking."

*June 2025*  
*Karim Elbakly*

# Contents

<b>1</b>	<b>Introduction</b>	<b>1</b>
<b>2</b>	<b>Entropy patch choked-nozzle interaction: Quasi-steady, inertial modeling regimes, and limits of linearization established</b>	<b>4</b>
2.1	Introduction	4
2.2	General approach	5
2.3	Reduced-order models	5
2.3.1	Matching condition model	5
2.3.2	Inertial model	7
2.4	Computational procedure	10
2.4.1	Mesh generation	11
2.4.2	Establishing choked-nozzle base flow	12
2.4.3	Entropy-patch choked-nozzle interaction simulations	13
2.5	Results & discussion	15
2.5.1	Use of reduced-order models for scaling analysis	15
2.5.2	Determination of the modeling regimes: Effect of entropy patch shape and size on the upstream acoustic response scaled by reduced-order models	16
2.5.3	Determining limits of linearized modeling: Effect of entropy-patch strength on upstream acoustic response prediction by reduced-order models	18
2.6	Conclusion	19
<b>3</b>	<b>Entropy-patch choked-nozzle interaction: Effects of nozzle convergent geometry on scaled upstream acoustic response</b>	<b>21</b>
3.1	Introduction	21
3.2	General approach	21
3.3	Computational procedure	22
3.3.1	Mesh Generation	22
3.3.2	Establishing choked-nozzle base flow	24
3.3.3	Entropy-patch choked-nozzle interaction simulations	24
3.4	Results & discussion	25
3.4.1	Effect of nozzle-inlet length ratio on the upstream acoustic response	25
3.4.2	Effect of nozzle contraction shape on the upstream acoustic response	28

3.4.3	Effect of nozzle contraction ratio on the upstream acoustic response . . . . .	31
3.5	Conclusion . . . . .	35
<b>4</b>	<b>Conclusions</b>	<b>37</b>
<b>A</b>	<b>Supporting derivations</b>	<b>39</b>
A.1	Derivation of Reflection coefficient at the nozzle throat . . . . .	39
A.2	Derivation of Eq. (2.31) . . . . .	40
A.3	Derivation of Eq. (2.32) . . . . .	41
A.4	A relation for the acoustic power emitted from the sound source . . . . .	41
A.5	Establishing choked-nozzle flow . . . . .	42
A.6	Derivation of Eq. (2.41) . . . . .	43
A.7	Generating entropy patches with similar relative excess density or excess mass . . . . .	43
<b>B</b>	<b>Supporting studies</b>	<b>45</b>
B.1	Pressure Signal Error Quantification . . . . .	45
	<b>References</b>	<b>47</b>

# List of Figures

2.1	Computational domain representation of nozzle with upstream channel	5
2.2	Unsteady pressure discontinuity in a uniform 1-D ducted flow emanating plane acoustic waves	7
2.3	Acoustic pressure waves emanating from a fluctuating pressure discontinuity located in the converging part of a choked-nozzle.	9
2.4	Schematic of multi-block numerical domain	11
2.5	Mach field of numerical domain resulting from intermediate run accompanied by the Mach profile along the symmetry line	13
2.6	Entropy field showing fully mature entropy patches	14
2.7	Dimensionless upstream observed acoustic response obtained from the inertial model accompanied by the Mach number along the symmetry line as a function of the dimensionless source position in the convergent part of the nozzle.	16
2.8	The maximum upstream acoustic response due to entropy-patch choked nozzle interaction obtained from numerical simulations scaled by the inertial model and the matching condition model as a function of dimensionless streamwise length scale $L_s/S_2$ .	17
2.9	The maximum upstream acoustic response due to entropy-patch choked nozzle interaction obtained from numerical simulations scaled by the inertial model and the matching condition model as a function of the entropy patch strength.	19
3.1	Nozzle convergent profiles used for investigating the effects of nozzle parameters on the upstream acoustic response due to entropy-patch choked-nozzle interaction.	23
3.2	Dimensionless upstream observed acoustic response obtained from the inertial model as a function of the dimensionless source position for nozzles with $C_r = 3$ and $N = 3$ at $L_r \in \{0.5, 1, 2, 3, 5\}$ .	26
3.3	The maximum upstream acoustic response due to entropy-patch choked nozzle interaction obtained from numerical simulations scaled by the inertial model as a function of dimensionless length scale $10L_s/L_c$ .	27
3.4	The maximum upstream acoustic response due to entropy-patch choked nozzle interaction obtained from numerical simulations scaled by the matching-condition model as a function of dimensionless length scale $L_s/2L_c$ .	28

3.5	(a) Dimensionless upstream observed acoustic response obtained from the inertial model as a function of the dimensionless source position for nozzles with $L_r = 0.5$ and $C_r = 3$ for $N \in \{2, 3, 4, 8\}$ . (b) Magnitude of centripetal acceleration as a function of the dimensionless position for nozzles with $L_r = 0.5$ and $C_r = 3$ for $N \in \{2, 3, 4, 8\}$ . . . . .	29
3.6	The maximum upstream acoustic response due to entropy-patch choked-nozzle interaction obtained from numerical simulations scaled by the inertial model as a function of the quasi-1D parameter. . . . .	30
3.7	The maximum upstream acoustic response due to entropy-patch choked-nozzle interaction obtained from numerical simulations scaled by the matching-condition model as a function of the quasi-1D parameter. . . . .	31
3.8	Dimensionless upstream observed acoustic response obtained from the inertial model as a function of the dimensionless source position for nozzles with $L_r = 3$ and $N = 3$ at $C_r \in \{1.25, 1.5, 3, 5, 7\}$ . . . . .	32
3.9	(a) Mach number as a function of the dimensionless position for nozzles with $L_r = 2$ and $N = 3$ at $C_r \in \{1.25, 1.5, 3, 5, 7\}$ . (b) Convective acceleration as a function of the dimensionless position for nozzles with $L_r = 2$ and $N = 3$ for $C_r \in \{1.25, 1.5, 3, 5, 7\}$ . . . . .	33
3.10	The maximum upstream acoustic response due to entropy-patch choked-nozzle interaction obtained from numerical simulations scaled by the inertial model as a function of the dimensionless streamwise length-scale $L_s/S_2$ for blocks with $10L_s/L_c = 1$ . . . . .	34
3.11	The maximum upstream acoustic response due to entropy-patch choked-nozzle interaction obtained from numerical simulations scaled by the matching-condition model as a function of the dimensionless streamwise length-scale $L_s/S_2$ for blocks with $L_s/2L_c = 2$ . . . . .	34
B.1	Measured upstream perturbation pressure signal at varying grid refinement levels. . . . .	46

# List of Tables

3.1	Entropy block generation settings used for the contraction ratio study.	25
B.1	Discretization error of upstream pressure perturbation due to entropy patch choked-nozzle interaction at different grid refinement levels. . .	46

# Summary

The effects of entropy-patch shape, size, and strength on the upstream acoustic response generated by entropy-patch choked-nozzle interactions are investigated. Numerical-simulation-based investigations, using a two-dimensional planar Euler code, reveal the existence of two distinct modeling regimes: the quasi-steady (matching-condition) regime and the inertial regime, respectively. The ratio of the entropy-patch streamwise length scale to the nozzle throat height was found to be an order parameter, which allows one to determine which of the two modeling regimes applies. Indeed, for entropy patches with a streamwise length scale smaller than or equal to the nozzle throat height, the inertial model provides a satisfactory prediction of the upstream acoustic response. For entropy patches with a streamwise length scale larger than the nozzle throat height, the matching condition model has superior predictive accuracy. The entropy patch's shape was judged to have only a slight impact on the applicable modeling regime. Additionally, the study examined entropy-patch strength using the ratio of area-specific perturbation energy to area-specific upstream energy as an order parameter, establishing that both of the above-mentioned linear models are only valid for weak entropy patches. Further investigation of the influence of nozzle geometry on the upstream acoustic response was conducted. A parametric study was carried out to quantify the effects of the nozzle convergent length ratio, contraction ratio, and profile shape on the reduced-order models' predictive accuracy. Entropy patches with a streamwise length scale much smaller relative to the nozzle convergent length were found to have better predictive accuracy by the inertial model. Whilst entropy patches with a streamwise length scale that is large relative to the nozzle convergent length were found to have better predictive accuracy by the matching-condition model. Furthermore, the inertial model was shown to have better agreement with simulations for nozzle convergent profiles that have a large radius of curvature and a height that varies gradually in the streamwise direction. The matching-condition model was found to be largely insensitive to the shape of the nozzle convergent profile. By changing the contraction ratio of the nozzle, it was found that the inertial model under-predicts acoustic responses for systems with an upstream Mach number above the compressible limit. The system's upstream Mach number was found not to affect the matching-condition model's predictive accuracy. These findings provide a framework for selecting appropriate models for entropy-patch choked-nozzle interaction scenarios, furthering the fundamental understanding of indirect noise-driven combustion instability.

# Chapter 1

## Introduction

Combustion noise has become a key topic in the context of propulsion and energy generation systems. This rise in importance was initiated by the need to reduce noise emissions to the environment, as it has been found to disturb human and/or animal life [1]. In recent years, the need to reduce greenhouse gas emissions to limit global warming as set by the UN Paris Agreement of 2016 [2] has driven the development of low-emission combustion technologies, such as lean premixed combustion, and the use of alternative fuels such as hydrogen. While these advancements contribute to reducing the environmental footprint of combustion systems, they also introduce new challenges related to combustion stability and noise generation.

One major challenge of using hydrogen as a fuel source is its tendency to burn more unsteadily compared to conventional hydrocarbon fuels. This increased combustion instability is primarily due to hydrogen's high reactivity, low ignition energy, and fast flame speeds [3]. Moreover, when employed in lean premixed combustors, hydrogen combustion typically operates near the lean blowout limit, which is beneficial for reducing emissions, but makes the system more susceptible to thermoacoustic instabilities, posing significant design and operational challenges [4–6].

Thermoacoustic instability refers to undesirable self-sustained pressure oscillations that arise from the coupling between a combustion-noise source and the acoustics of the combustor [7–9]. These instabilities not only limit the operational range of combustion systems, necessitating conservative design margins to avoid flame blow-off and flashback [10], but can also lead to severe structural damage in the combustion chamber, potentially resulting in critical system failure [11].

Acoustic pressure fluctuations can be attributed to direct noise and indirect noise. The direct noise sources are related to the unsteady processes of volumetric expansion and contraction of the flame. Indirect sources refer to sound production in wall-bound combustion resulting from the interaction of non-uniform flow features, such as entropy patches or vortices, with the combustion chamber exit.

Direct noise sources have been widely studied [7, 8, 12, 13]. In contrast, indirect noise has received less attention—especially voriticity noise [14]. However, Duran and Moreau [15] as well as Leyko et al. [16] assert that in real (industrial) combustion systems, indirect combustion noise can be of orders of magnitude greater than direct combustion noise.

In order to cultivate fundamental understanding of complex phenomena such as

indirect combustion noise, it is standard practice to perform order-reduction by designing experiments in which only one effect is dominant—or on occasion, when the former has been done, a few effects [14, 17–24]. A prime example of this approach are Anthoine’s et al. [17] cold-gas (without combustion) scale-model experiments, which were used to investigate self-sustained pressure pulsations in solid-rocket motors. Indeed, these demonstrated the importance of the integrated nozzle’s nozzle-cavity volume on indirect noise produced by essentially nonlinear azimuthal-vortex-nozzle (or ring-vortex-nozzle) interaction. Other examples are Bake’s et al. [18] canonical entropy-noise experiment, De Domenico’s et al. experiment [22], Noiray & Wellemann’s experiment [23], and Hirschberg’s et al. entropy & axial-component-vorticity noise experiments [14, 21, 24]. Moreover, the practice of studying indirect combustion-noise sources in isolation has also been successfully used for the development of analytical & numerical indirect combustion-noise models [25–29].

Of the two indirect combustion-noise sources, entropy noise has been the most widely studied, as evidenced by the high number of citations of two seminal articles by Marble & Candel [25] and Ffowcs Williams & Howe [26]. Marble & Candel’s one-dimensional (1-D) modeling approach [25, 26], based on the notion of plane entropy-wave interaction with a nozzle, appears to be the most widely applied. In contrast, Ffowcs Williams & Howe’s modeling approach considers, three-dimensional patches of the fluid—with relative-excess mass—convected by the flow [26].

Ffowcs Williams & Howe seem to have argued that “*to elicit in detail the physical mechanisms responsible for the generation of sound*” [26] the inclusion of acceleration/unsteadiness is an ineluctable ingredient for a model. Whereas, Marble & Candel astutely pointed out: “*When the scale of the disturbance impinging upon the nozzle is large in comparison with the nozzle length ... the response of the nozzle is well approximated by a matching-condition analysis. Though limited in the range of frequency over which it is applicable, the results which follow from this approximation are simple and extremely useful. The idea is simply that, to disturbances of very long wavelength, the nozzle appears as a discontinuity in the state of the medium supporting the propagation; the state gradients ... become discontinuities. The nozzle then provides matching conditions between uniform upstream and downstream states, which may be derived from conservation laws and the geometric description of the nozzle.*”

For the case of choked-nozzle-flow experiments, Hirschberg et al. [14] used Marble & Candel’s above-quoted observation to formulate a bare-bones matching-condition model. Said model was validated by comparison with Leyko’s et al. [27] simulation results [14]. Moreover, Hirschberg et al. [14] pointed out that in the cases where matching-condition modeling is applicable: sound production is due to a temporary axial mass-flow rate change caused by the passage of an entropy patch through the nozzle throat.

Given that Ffowcs Williams & Howe’s [26] method is not limited to a single spatial dimension, it allows for the investigation of the entropy-patch size on sound production. Ffowcs Williams & Howe [26] investigated the influence of entropy-patch size on sound generation, which they termed “*acoustic bremsstrahlung*” or “*bremsstrahlung*” [26]. In particular, they used their model to compare the sound generation of a duct-sized entropy “*slug*” to that of a much smaller spherical “*pellet*,”

as these pass through a duct contraction or a nozzle [26]. One should note that Ffowcs Williams & Howe only considered low-Mach-number flow; viz., they did not consider choked-nozzle flows.

In the present study, inspired by Marbel & Candel [25] and Ffowcs Williams & Howe's [26] work, but with a focus on choked-nozzle flows, we investigated the influence of an entropy-patch shape, size, and strength as well as the effects of the nozzle geometry on the upstream-traveling acoustic response due to entropy-patch choked-nozzle interaction using numerical simulations. Where linear reduced-order model-based scaling rule analysis was performed on the results. It builds on the work of Kowalski et al. [30]. They established the existence of two modeling regimes [30]:

- The inertial regime where the acceleration of an entropy patch is the governing contribution to sound production.
- A quasi-steady modeling regime, in which sound production is due to the modulation of the volumetric flux through the nozzle throat. Kowalski et al. [30] refer to this regime as the matching condition regime.

Kowalski et al. [30] determined that small entropy patches are in the inertial regime. Whilst the matching-condition modeling applies to large entropy patches. It should be noted that Kowalski's et al. [30] analysis relied on linearization.

The fundamental questions that we aimed to answer were:

1. Are there dimensionless order parameters that allow one to determine if one finds oneself in either the inertial modeling or the matching-condition regime?
2. Is there a dimensionless order parameter that allows one to determine if linearization is an appropriate modeling strategy and when nonlinearity becomes essential?
3. What is the influence of a nozzle's geometry on sound production due to entropy-patch choked-nozzle interaction?

Questions 1 & 2 are addressed in chapter 2. Work performed to answer the third question is presented in chapter 3.

# Chapter 2

## Entropy patch choked-nozzle interaction: Quasi-steady, inertial modeling regimes, and limits of linearization established

### 2.1 Introduction

Understanding the mechanisms that govern indirect noise generation in propulsion systems is a critical step in the development of reliable low-emission combustion technologies. Building on the preliminary work by Kowalski et al. [30, 31], which investigated entropy-patch interactions with choked nozzles using a two-dimensional (2-D) planar Euler code tailored for internal flow acoustics (EIA) developed by Hulshoff [32], this chapter aims to systematically investigate the modeling regimes applicable to such interactions. While Kowalski's efforts laid important groundwork, their results were limited by unquantified numerical errors, low signal-to-noise ratios, and approximated key parameters.

To overcome these limitations, the present study employs a significantly improved numerical simulation strategy developed by Elbakly [33], which improves the signal-to-noise ratio. Indeed, it allowed us to simulate interactions involving smaller entropy patches than was possible using Kowalski's et al. approach [30, 31]. Furthermore, the modified EIA code allows for direct extraction of critical quantities such as excess mass, excess-mass density, and convective acceleration, parameters essential for reduced-order model analysis. Additionally, Kowalski et al. [30, 31] did not find the appropriate dimensionless order parameters, which allow one to differentiate between the inertial & matching-condition regimes, and linear & nonlinear regimes.

This chapter investigates the applicability of two reduced-order models, the quasi-steady matching-condition model and the inertial mode, for predicting the upstream acoustic response resulting from entropy-patch choked-nozzle interactions. Particular emphasis was placed on identifying dimensionless order parameters that distinguish between the two modeling regimes and define the limits of linearized modeling.

## 2.2 General approach

To investigate the limits of the matching-condition & inertial model, numerical simulations were carried out using EIA [32]. The pressure pulsations, due to entropy-patch choked-nozzle interaction, obtained from the numerical simulations were scaled using the reduced-order models; viz., the matching-condition & inertial models. The computational domain used throughout the study can be seen in Fig. 2.1. The computational domain consists of a nozzle with a throat height of  $2S_2$  and a depth of  $2S_1$  connected to an upstream chamber with a channel height of  $2S_1$  and depth  $2S_1$ .

The reduced-order models are presented in §2.3. The computational procedure used is presented in §2.4.

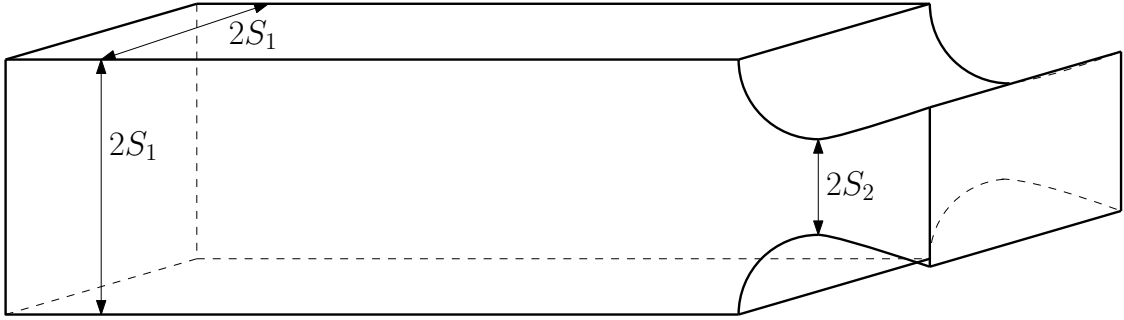


FIGURE 2.1: Computational domain representation of nozzle with upstream channel [34]

## 2.3 Reduced-order models

In this section, two bare-bones models are derived for the prediction of an upstream acoustic pressure response due to an entropy patch interacting with a choked-nozzle. The first model will be referred to as the matching-condition model, it is based on the quasi-steady analysis of Marble & Candel [25]. The second model, inspired by Ffowes Williams & Howe’s analytical model [26], will be referred to as: the inertial model.

### 2.3.1 Matching condition model

Here the derivation of a matching condition model, for the prediction of upstream acoustic pressure response  $p'_u$ , due to the interaction of an entropy patch of excess density  $\rho'_e = \rho_e - \rho_u$  with a choked nozzle is provided, where  $\rho_u$  is the density of the upstream channel and  $\rho_e$  is the density of the entropy patch. Upstream from the nozzle, the flow is taken to be one-dimensional (1-D) viz., the local flow variables vary only in the streamwise direction. Additionally, it is assumed that  $\rho'_e/\rho_u$  is small enough, such that the entropy patch is carried by the base flow without affecting it. Lastly, it is assumed that the interaction time scale of the entropy patch with the nozzle is significantly larger than the travel time of a material element through the nozzle.

Now, let us consider d'Alembert's solution to the one-dimensional wave equation:

$$p' = p^+(x - (c + u)t) + p^-(x + (c - u)t) \quad (2.1)$$

$$u' = u^+(x - (c + u)t) + u^-(x + (c - u)t) \quad (2.2)$$

where  $p^\pm$  and  $u^\pm$  are pressure & velocity perturbations (the subscripts + and - denote downstream and upstream traveling waves) at a position  $x$  at time  $t$  and  $c$  is the sound speed. If one considers an infinite duct with anechoic terminations and only perturbations traveling in the upstream direction, the equations reduce to the following:

$$p' = p^-(x + (c - u)t) \quad (2.3)$$

$$u' = u^-(x + (c - u)t) \quad (2.4)$$

Applying the above equations to the linearized one-dimensional momentum conservation equation

$$\rho_u \frac{\partial u'}{\partial t} = -\frac{\partial p'}{\partial x} \quad (2.5)$$

one finds that the upstream pressure perturbation  $p'_u$  can be written as follows:

$$p'_u = -\rho_u c_u u'_u \quad (2.6)$$

The upstream velocity perturbation  $u'_u$  can be found by considering the upstream Mach number:

$$M_u = \frac{u_u}{c_u} \quad (2.7)$$

which is constant for a choked-nozzle flow. Thus, taking the total derivative

$$d(M_u) = d\left(\frac{u_u}{c_u}\right) = 0 \quad (2.8)$$

one finds the following relation

$$\frac{u'_u}{u_u} = \frac{c'_u}{c_u} \quad (2.9)$$

Assuming the fluid in the system to be a perfect gas, the speed of sound can be written as

$$c_u^2 = \gamma \frac{p_u}{\rho_u} \quad (2.10)$$

where  $\gamma = c_p/c_v$  is the ratio of heat capacities at constant pressure and volume, respectively. Taking the total derivative of this expression yields

$$d(c_u^2) = \frac{\gamma}{\rho_u} d(p_u) + \gamma p_u d\left(\frac{1}{\rho_u}\right) \quad (2.11)$$

If one assumes isobaric generation of an entropy patch, one finds:

$$2 \frac{c'_u}{c_u} = -\frac{\rho'_u}{\rho_u} = -\frac{\rho'_e}{\rho_u} \quad (2.12)$$

Using this relation and Eq. 2.9 to rewrite the velocity perturbation in Eq. 2.6, allows one the find:

$$\boxed{p'_u = \frac{1}{2} \rho_u c_u u_u \left(\frac{\rho'_e}{\rho_u}\right) = \frac{1}{2} \rho_u c_u^2 M_u \left(\frac{\rho'_e}{\rho_u}\right) = \frac{1}{2} \gamma p_u M_u \left(\frac{\rho'_e}{\rho_u}\right)} \quad (2.13)$$

where  $p_u = \rho_u c_u^2 / \gamma$  is the static pressure of the upstream channel. Hereon, this quasi-steady model will be referred to as the matching-condition model.

### 2.3.2 Inertial model

In this section, the derivation of an inertial model inspired by Ffowcs Williams & Howe's analytical model [26] is provided.

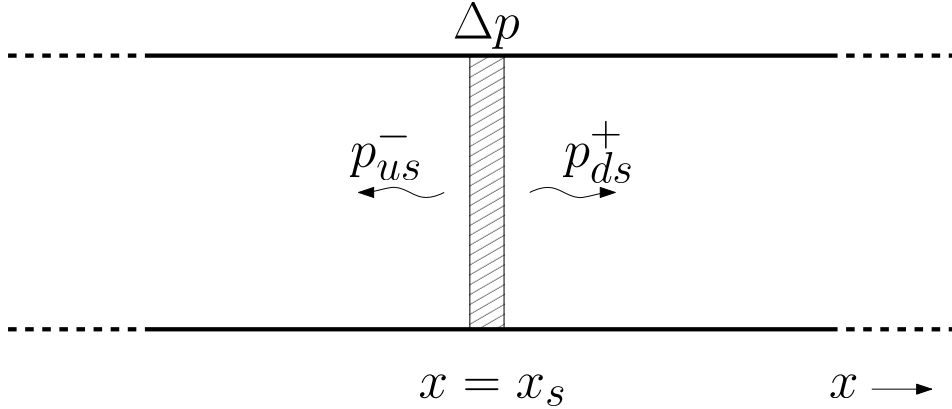


FIGURE 2.2: Unsteady pressure discontinuity  $\Delta p$  at  $x = x_s$ , in a uniform 1-D ducted flow emanating plane acoustic waves  $p_{us}^-$  and  $p_{ds}^+$ .

Consider a sound source in the form of an unsteady pressure discontinuity  $\Delta p$  at a position  $x = x_s$  (Fig. 2.2). It is assumed that said pressure discontinuity is present in a duct with a uniform cross-section and 1-D flow with Mach number  $M$ . Given that the pressure discontinuity is unsteady: pressure waves emanate from it in the upstream  $p_{us}^-$  and downstream  $p_{ds}^+$  direction. Here the subscripts  $us$  and  $ds$  indicate perturbations upstream and downstream relative to the sound

source. The superscripts  $-$  and  $+$  denote downstream and upstream traveling waves, respectively.

Assuming an infinite duct with anechoic terminations,  $\Delta p$  can be expressed in terms of the emitted pressure perturbations as follows:

$$\Delta p = p_{ds}^+ - p_{us}^- \quad (2.14)$$

The mass flux across the pressure discontinuity is conserved, and thus one can write

$$(\rho u)'_{ds} = (\rho u)'_{us} \quad (2.15)$$

which can be re-written as

$$\rho_{ds}^+ u + \rho u_{ds}^+ = \rho_{us}^- u + \rho u_{us}^- \quad (2.16)$$

where the terms without sub or superscripts are the mean flow variables (higher-order perturbation terms are neglected).

For an isentropic flow, the density perturbations can be expressed as:

$$\rho^\pm = \frac{p^\pm}{c^2} \quad (2.17)$$

Using d'Alembert's solution to the one-dimensional wave equation and the linearized one-dimensional momentum conservation equation, the velocity perturbations can be expressed as

$$u^\pm = \pm \frac{p^\pm}{\rho c} \quad (2.18)$$

Using Eq. 2.17 & Eq. 2.18 to re-write the perturbation terms in Eq. 2.16, one finds

$$p_{ds}^+(1 + M_s) = p_{us}^-(-1 + M_s) \quad (2.19)$$

where  $M_s$  is the Mach number at the sound source. Using Eq. 2.14 the pressure perturbations can be written as

$$p_{us}^- = -\frac{1 + M_s}{2} \Delta p \quad (2.20)$$

$$p_{ds}^+ = \frac{1 - M_s}{2} \Delta p \quad (2.21)$$

This result will be applied to the subsonic parts of a choked-nozzle with varying cross-sectional area  $A = A(x)$ . Here it is assumed that the nozzle is quasi-1-D; viz., the rate of change of the cross-sectional area is considered to be very small [35].

At the nozzle throat, we assume that downstream traveling waves are reflected. Thus, an additional upstream traveling perturbation  $p_{ds}^-$  is to be accounted for downstream from  $\Delta p$  (Fig. 2.3). The reflection coefficient at  $x = x_{th}$  can be taken as (Appendix A.1)

$$R = \frac{1 - \frac{\gamma-1}{2} M_s}{1 + \frac{\gamma-1}{2} M_s} \quad (2.22)$$

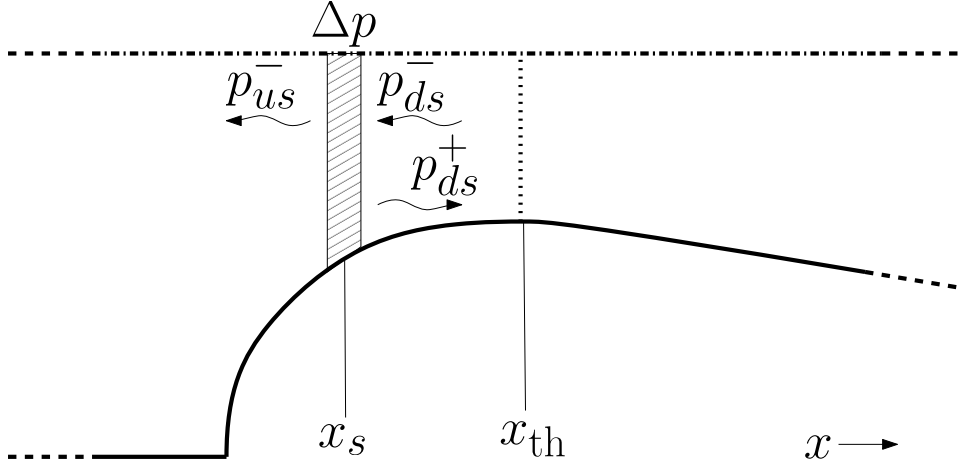


FIGURE 2.3: Acoustic pressure waves emanating from a fluctuating pressure discontinuity  $\Delta p$  located at  $x = x_s$  in the converging part of a choked-nozzle. As the nozzle is choked and the flow is 1D, one has sonic line at  $x = x_{th}$ , viz., at the throat.

Thus,  $p'_{us}$  can be expressed as follows:

$$p'_{us} = p_{us}^- + p_{ds}^- = p_{us}^- + R p_{ds}^+ \quad (2.23)$$

which using Eq. 2.20 and Eq. 2.21 can be expressed as follows:

$$p'_{us} = -\frac{\Delta p}{2} ((1 + M_s) - R(1 - M_s)). \quad (2.24)$$

To find the pressure perturbation observed in the upstream channel due to an upstream traveling pressure wave  $p'_u$  at location  $x = x_u$ , one must account for the change in cross-sectional area  $A$ . The acoustic power emitted directly upstream of the sound source can be taken as (Appendix A.4)

$$|\Phi_s^-| = \frac{A_s}{\rho_s c_s} |p'_{us}|^2 (1 - M_s)^2 \quad (2.25)$$

and at the observer position, the acoustic power can be expressed as

$$|\Phi_u^-| = \frac{A_u}{\rho_u c_u} |p'_u|^2 (1 - M_u)^2. \quad (2.26)$$

Given that we consider an isentropic system, it must hold true that  $|\Phi_s^-| = |\Phi_u^-|$ . This allows one to express the magnitude of the observed pressure perturbation as:

$$|p'_u| = \sqrt{\frac{\rho_u c_u}{\rho_s c_s} \frac{A_s}{A_u}} ((1 + M_s) - R(1 - M_s)) \left( \frac{1 - M_s}{1 - M_u} \right) \frac{\Delta p}{2}. \quad (2.27)$$

Noting that an unsteady force from a wall on the fluid is a sound source [36, 37], we write

$$\Delta p = \frac{F_x}{A_s} \quad (2.28)$$

where the force  $F_x$  is exerted by the walls of the nozzle inlet on the fluid.  $F_x$  is due to the acceleration of an entropy patch, which is taken to be a point particle with an excess mass  $m_e$ . i.e., one can write

$$F_x = m_e \left( u \frac{du}{dx} \right). \quad (2.29)$$

Using the above, Eq. 2.27 can be re-written as follows:

$$\boxed{|p'_u| = \sqrt{\frac{\rho_u c_u}{\rho_s c_s} \frac{1}{A_u A_s}} \left( (1 + M_s) - R(1 - M_s) \right) \left( \frac{1 - M_s}{1 - M_u} \right) \frac{m_e}{2} \left( u \frac{du}{dx} \right)} \quad (2.30)$$

Using Bernoulli's principle and isentropic perfect gas relations, the  $\sqrt{\rho_u c_u / \rho_s c_s}$  and  $A_s$  terms in the above equation can be expressed as follows (Appendices A.2 and A.3):

$$\sqrt{\frac{\rho_u c_u}{\rho_s c_s}} = \left( \frac{1 + \frac{\gamma-1}{2} M_s^2}{1 + \frac{\gamma-1}{2} M_u^2} \right)^{\frac{\gamma+1}{4(\gamma-1)}} \quad (2.31)$$

and

$$A_s = \frac{A_{th}}{M_s} \left( 1 + \frac{\gamma-1}{\gamma+1} (M_s^2 - 1) \right)^{\frac{\gamma+1}{2(\gamma-1)}}. \quad (2.32)$$

where the cross-sectional area of the throat is taken to be  $A_{th} = 4S_1 S_2$  (Fig. 2.1). Going forward, Eq. 2.30 will be referred to as the inertial model.

## 2.4 Computational procedure

Parametric studies of entropy-patch choked-nozzle interaction were carried out using Hulshoff's two-dimensional Euler Internal Aeroacoustics code (EIA) [32]. EIA makes use of the compressible lossless governing (Euler) equations given by

$$\frac{\partial \rho}{\partial t} + \nabla \cdot (\rho \mathbf{u}) = 0 \quad (2.33)$$

$$\frac{\partial \rho \mathbf{u}}{\partial t} + \nabla \cdot (\rho \mathbf{u} \mathbf{u} + p \mathbf{I}) = \rho \mathbf{F}_E \quad (2.34)$$

$$\frac{\partial E_T}{\partial t} + \nabla \cdot ((E_T + p) \mathbf{u}) = Q_E \quad (2.35)$$

to resolve the domain, where  $E_T = \rho(e + |\mathbf{u}|^2/2)$  is the total energy density,  $\rho \mathbf{F}_E$  is an external momentum source density, and  $Q_E$  is an external energy source.  $\mathbf{F}_E$  can be used to generate vortices as previously done by Hulshoff et al. [38] & Hirshberg et al. [28, 39, 40]. For the purposes of this study,  $Q_E$  is of greater interest as it can be used to generate entropy patches, as will be discussed in §2.4.3.

The computational procedure used to carry out the numerical study is the same as reported by Elbakly [33]. It consists of three sequential steps:

1. Generation of a computational mesh (detailed in §2.4.1).
2. Establishing steady choked-nozzle base flow (expanded upon in §2.4.2).
3. Running unsteady entropy-patch-choked-nozzle-interaction (ECNI) simulations (discussed in §2.4.3).

### 2.4.1 Mesh generation

In this section, details regarding mesh generation are provided for the convergent-divergent-nozzle configuration used for the present study.

The schematic of the numerical domain used can be seen in Fig. 2.4. The domain utilizes a multi-block system where blocks B1, B2, B3, and B4 are used for carrying out the numerical computations. Block B5 is a (passive) 1-D extraction region used to ensure only planar acoustic waves are recorded—note that block B5 is a post-processing block and does not affect any of the adjacent blocks [32].

The upstream channel is defined by block B3 with a height  $S_1 = 1$  m, in which entropy patches are generated and convected downstream. Block B2 acts as a transition zone to minimize cell stretching and skew. The convergent part of the nozzle (nozzle inlet) is Block B1. The nozzle inlet curve was generated using a Henrici transform [41] as previously done by Hirshberg [34], with a contraction ratio  $S_1/S_2 = 3$  and length ratio  $L_c/S_1 = 1/2$ . Lastly, downstream on the contraction block, B4 acts as the diffuser. Note that the geometry of the diffuser is not of high importance, as only choked-nozzle flow is considered, implying a supersonic condition in the diffuser, preventing the travel of information upstream.



FIGURE 2.4: Schematic of multi-block numerical domain with  $S_1/S_2 = 3$

To establish appropriate levels of grid resolution, a discretization error study was carried out (Appendix B.1). In which base flows were established using a four-stage second-order accurate (4,2) Runge-Kutta scheme for time discretization and a second-order total-variation-diminishing (TVD) Roe approximate Riemann solver with a van Leer limiter for space discretization. ECNI simulations were done using a five-stage second-order accurate (5,2) Runge-Kutta scheme for time discretization and a second-order total-variation-diminishing (TVD) Roe approximate Riemann solver with a van Leer limiter for space discretization. It was established that using a grid resolution of 30 points per circular entropy spot radius  $R_s$  or rectangular block half-width  $W_s$  gives a discretization error of 2.2% at an observed order of accuracy of 1.9 at a distance  $42R_s/W_s$  away from the nozzle inlet. Ergo, for the current study, meshes were generated using a base value of 30 points per length scale of the entropy patch.

## 2.4.2 Establishing choked-nozzle base flow

In this section, the computational procedure used to establish a base flow with a choked-nozzle condition is briefly discussed; for an expansive explanation, the reader is referred to Elbakly's report [33].

Elbakly's computation procedure [33] makes use of a pre-established steady base flow to initialize the flow field for the unsteady ECNI simulation. To establish this base flow, two separate numerical runs are required. An initial condition run is performed to establish a choked-nozzle flow, followed by an intermediate run to homogenize the flow field and ensure the passing of transients arising from changing boundary conditions between the initial condition run and the ECNI run.

For the initial condition run the flow field was initialized by setting the blocks upstream of the nozzle throat (B1, B2, B3, & B5) to have density  $\rho = 1 \text{ kg} \cdot \text{m}^{-3}$ , specific heat ratio  $\gamma = 1.4$ , pressure  $p = c^2\rho/\gamma \approx 0.7 \text{ kg} \cdot \text{s}^{-2} \cdot \text{m}^{-1}$ , and velocity  $\mathbf{U} \equiv (U_{\text{des}}, 0)^T \approx (0.2, 0) \text{ m} \cdot \text{s}^{-1}$ .  $U_{\text{des}}$  is the imposed inlet velocity needed to establish a choked-nozzle flow for the given contraction ratio [35]. Block B4 downstream of the nozzle throat was initialized by setting  $\rho = 1.0 \text{ kg} \cdot \text{m}^{-3}$ ,  $\gamma = 1.4$ ,  $p = c^2\rho/2\gamma \approx 0.4 \text{ kg} \cdot \text{s}^{-2} \cdot \text{m}^{-1}$ , and  $\mathbf{U} \equiv (1, 0)^T \text{ m} \cdot \text{s}^{-1}$ . Note that for the whole domain, the local speed of sound  $c$  was assumed to be one as per the definition of pressure. Block B4 was set to have a pressure two times lower than that of the upstream blocks to ensure no shockwaves are formed in the diffuser <sup>1</sup>.

For the initial condition run, a constant inflow condition was set on the left bound of blocks B3 and B5 maintaining  $\rho = 1.0 \text{ kg} \cdot \text{m}^{-3}$ ,  $\mathbf{U} \equiv (0.2, 0)^T \text{ m} \cdot \text{s}^{-1}$  and  $c = 1 \text{ m} \cdot \text{s}^{-1}$ . Pressure relief surfaces on the upper and lower bounds of block B3 were imposed by setting  $R \equiv p^-/p^+ = 0$ . Wall boundary conditions were imposed on the lower bounds of blocks B1, B2, and B4. On the upper bounds of blocks B1, B2, and B4, symmetry boundary conditions were imposed. Non-reflective boundary conditions are applied on the right bound on block B4 to imitate anechoic termination. A 1-D boundary condition on the upper and lower bound of block B5 was imposed to classify the block as a post-processing block. Extraction boundary conditions were applied on the interface between blocks B3 and B5 to ensure an omnidirectional transfer of information from block B3 to B5. Connection boundary conditions were applied to the remaining block interfaces to allow for the transfer of data between blocks.

After the domain was fully defined, simulations were initiated and ran until they fully converged. A Roe-TVD scheme with a Van Leer limiter was used for spatial discretization. Temporal discretization was done by means of a second-order accurate four-stage (4,2) Runge-Kutta scheme with alpha coefficients (0.240, 0.375, 0.5, 1.0) and a max Courant limit of one, with artificial dissipation running on the first stage. Time marching was done using a non-time-accurate method, as one is interested in the steady state solution.

The converged solution of the initial condition run was used to initialize the domain for the intermediate run. For the intermediate run, some of the boundary

---

<sup>1</sup>The formation of shockwaves does not negatively affect the upstream recorded signal as one has a sonic condition at the throat preventing the travel of flow features upstream. However, the formation of shockwaves negatively impacts the computation time by reducing the allowable time step.

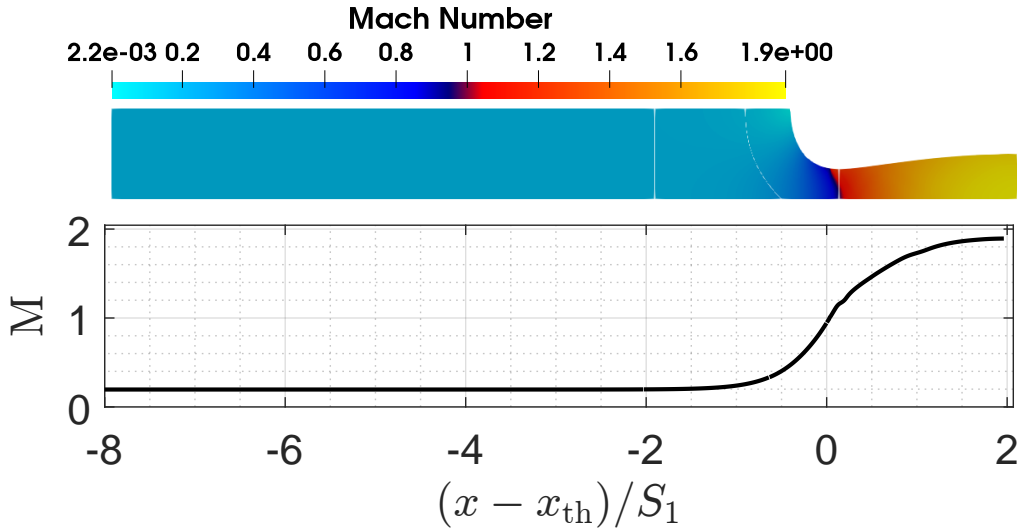


FIGURE 2.5: Mach field of numerical domain resulting from intermediate run accompanied by the Mach profile along the symmetry line ( $M_u \approx 0.2$ ).

conditions are altered. For instance, the constant inflow boundary conditions imposed on the left bounds of blocks B3 and B5 are replaced by non-reflective boundary conditions to imitate anechoic terminations [Note that removing inflow boundary conditions does not halt flow in the numerical domain as EIA makes use of the Euler equations which are lossless]. Furthermore, the pressure relief wall conditions applied to the upper and lower bounds of block B3 are replaced with symmetry & wall symmetry boundary conditions. The intermediate run was matched to full convergence using the same numerical methods as used for the initial condition run.

The flow field resulting from the intermediate run and the associated Mach profile along the symmetry line is shown in Fig. 2.5. One notes that the upstream chamber is uniform and has a Mach number  $M_u \approx 0.2$ .

### 2.4.3 Entropy-patch choked-nozzle interaction simulations

In this section, the computational procedure used to carry out ECNI runs is discussed. Additionally, the most important aspects of entropy-patch generation are expanded upon.

The ECNI run uses the flow field resulting from the intermediate run to initialize the flow field, using the same boundary conditions. The differences between the intermediate run and the ECNI run are as follows:

- The placement and use of a data-recording probe in the 1-D extraction region at a distance  $10S_1$  from the nozzle inlet. This pressure probe was set to record density, pressure, velocity, and temperature.
- The numerical methods used to resolve the flow field. The ECNI run makes use of a Roe-TVD scheme with a Van Leer limiter for spatial discretization. For temporal discretization, a second-order accurate five-stage (5,2) Runge-Kutta scheme with alpha coefficients (0.125, 0.1666, 0.375, 0.5, 1.0) with artificial

dissipation set to run only on the first two stages. A time-accurate method was used with a maximum Courant limit of two.

- The generation of entropy patches on top of the background flow. This is expanded upon in the remainder of this subsection.

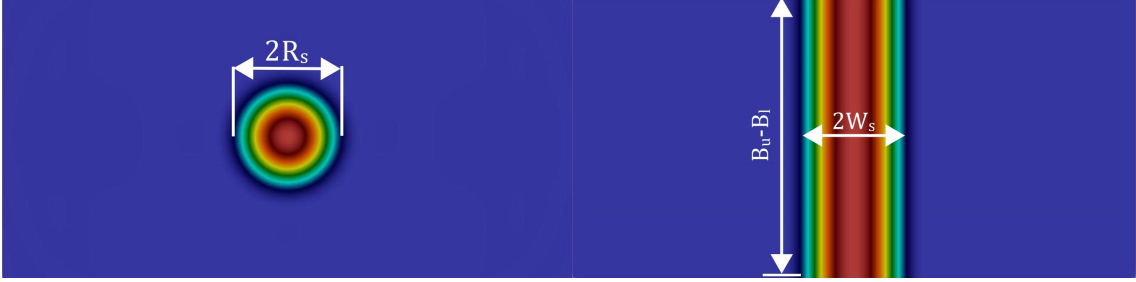


FIGURE 2.6: Entropy field showing fully mature entropy patches; entropy spot (right), entropy block (left).

As mentioned above, entropy patches were generated using the  $Q_E$  term in Eq. 2.35. In EIA, this is done by means of direct energy injection around a moving reference point [the reference point is normally set to move with background flow] with a local distribution of  $Q_E$  in the energy balance equation, which influences local entropy generation. One can generate two types of entropy patches: entropy spots (circular patches) and blocks (rectangular slug-like patches). For both these patches we identify a characteristic streamwise length scale, see Fig. 2.6. In the case of an entropy spot it is the radius of the spot  $R_s$ , and for an entropy block it is the half-width of the block  $W_s$ .

$Q_E$  is defined as a function of the generation amplitude  $A_{\text{gen}}$  and the distance from the center of the generation region  $\zeta$  in the direction of the length scale. For entropy spots the source term is defined as follows:

$$Q_E = \begin{cases} \frac{A_{\text{gen}}}{2} \left( 1 + \cos \left( \pi \frac{\zeta}{R_s} \right) \right) & \text{if } \zeta \in [0, R_s] \\ 0 & \forall \zeta \notin [0, R_s] \end{cases} \quad (2.36)$$

and for entropy blocks the source term is

$$Q_E = \begin{cases} A_{\text{gen}} \cos \left( \frac{\pi}{2} \frac{\zeta}{W_s} \right)^2 & \text{if } \zeta \in [0, W_s] \text{ and } [B_l, B_u] \\ 0 & \forall \zeta \notin [0, W_s] \text{ and } [B_l, B_u] \end{cases} \quad (2.37)$$

where  $B_l$  and  $B_u$  are the lower and upper bounds of the generation region. The generation amplitude is time-dependent and is defined as follows:

$$A_{\text{gen}} = \begin{cases} \frac{A_{\text{max}}}{2} \left( 1 - \cos \left( \frac{\pi t}{\tau_{\text{start}}} \right) \right) & \text{if } t \in [0, \tau_{\text{start}}], \\ A_{\text{max}} & \text{if } t \in (\tau_{\text{start}}, \tau_{\text{start}} + \tau_{\text{max}}] \\ \frac{A_{\text{max}}}{2} \left( 1 + \cos \left( \frac{\pi(t - (\tau_{\text{start}} + \tau_{\text{max}}))}{\tau_{\text{end}}} \right) \right) & \text{if } t \in (\tau_{\text{start}} + \tau_{\text{max}}, \tau_{\text{start}} + \tau_{\text{max}} + \tau_{\text{end}}] \\ 0 & \text{if } t \in (\tau_{\text{start}} + \tau_{\text{max}} + \tau_{\text{end}}, t_{\text{end}}) \end{cases} \quad (2.38)$$

where  $t$  is the time,  $A_{\text{max}}$  the maximum generation amplitude,  $\tau_{\text{start}}$  the ramp-up time of entropy generation,  $\tau_{\text{max}}$  the generation time at max amplitude, and  $\tau_{\text{end}}$  the wind-down time. Note that  $R_s$ ,  $W_s$ ,  $B_u$ ,  $B_l$ ,  $A_{\text{max}}$ ,  $\tau_{\text{start}}$ ,  $\tau_{\text{max}}$ ,  $\tau_{\text{end}}$  are user-set variables.

All entropy patches (spots and blocks) used for the current study were generated with the same  $A_{\text{gen}}/A_{\text{max}}$  profile; viz.,  $\tau_{\text{start}} = \tau_{\text{end}} = 6$  s and  $\tau_{\text{max}} = 3$  s. Entropy spots were generated with their reference point moving along the symmetry line. The entropy blocks were generated with their upper and lower bounds coinciding with the upper and lower bounds on the numerical domain. Furthermore, it was ensured that the entropy patches were fully mature before they left the generation block B3 such that there was no overlap between the pressure perturbations due to entropy generation and entropy-patch choked-nozzle interaction.

## 2.5 Results & discussion

### 2.5.1 Use of reduced-order models for scaling analysis

#### Matching-condition model-based scaling

The matching-condition model requires the relative excess density ( $\rho'_e/\rho_u$ ) of the entropy patch. In the cases considered here, entropy patches have an excess density  $\rho'_e < 0$ . The relative excess density was approximated as follows:  $(\rho'_e/\rho_u) \simeq -|\rho'_e/\rho_u|_{\text{max}}$ .

For each simulation  $|\rho'_e/\rho_u|_{\text{max}}$  is determined using an EIA functionality developed by Elbakly [33]. Its value is then substituted in Eq. 2.13 to determine  $p'_{\text{matching}}$ , which is then used to scale the simulation results. This was done to determine if the generated upstream acoustic response is due to a quasi-steady mechanism. I.e., it was, on a case-by-case basis, used to establish whether or not the ECNI results were in the matching-condition modeling regime.

#### Inertial model based scaling

The convective acceleration  $u(du/dx)$ , needed as an input for the inertial model, was extracted along the symmetry line from the flow field established during the intermediate run. Using  $u(du/dx)$ , we determined the dimensionless upstream acoustic response  $|p'_u|S_1^3/(m_e U_u^2)$  as a function of dimensionless sound-source location  $(x_s - x_{\text{th}})/L_c$  in the convergent part of the quasi-1-D nozzle (see Fig. 2.7). One notes

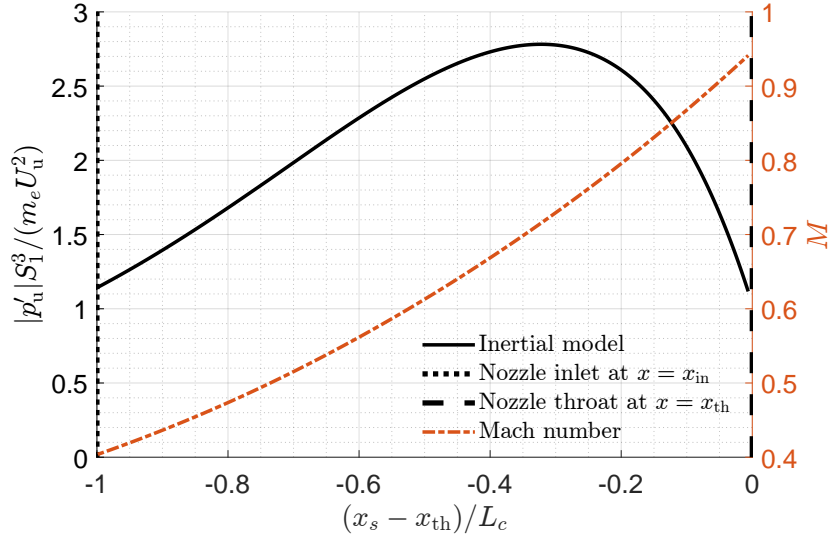


FIGURE 2.7: Dimensionless upstream observed acoustic response  $|p'_u| S_1^3 / (m_e U_u^2)$  obtained from the inertial model (right axis) and Mach number  $M$  along the symmetry line (left axis) as a function of the dimensionless source position  $(x_s - x_{th})/L_c$  in the convergent part of the nozzle.

that there is a maximum in dimensionless acoustic response at  $(x_s - x_{th}) = 0.32L_c$ . Going forward, we will refer to this predicted maximum amplitude as  $p'_{inertial}$ . For a fixed nozzle geometry, which we consider here,  $p'_{inertial}$  is determined by the excess mass  $m_e$  carried by the entropy patch. Thus, one can estimate the  $p'_{inertial}$  for a given simulation by extracting  $m_e$ . This is done using a purposely developed EIA functionality [33]. Note that EIA is a planer 2-D code meaning that the value of the excess mass obtained from it  $m_{e,EIA}$  is in  $kg \cdot m^{-1}$  and should be scaled by the depth of the computational domain (Fig. 2.1),  $m_e = 2S_1 m_{e,EIA}$ , to be used in the inertial model.

To determine whether the upstream acoustic-response amplitude  $|p'_u|$  resulting from an ECNI run is due to the acceleration of the patch, it is scaled by  $p'_{inertial}$ . In other words,  $|p'_u|/p'_{inertial}$  is computed for each ECNI run to determine whether or not the relevant sound-production mechanism is in the inertial modeling regime.

## 2.5.2 Determination of the modeling regimes: Effect of entropy patch shape and size on the upstream acoustic response scaled by reduced-order models

To judge whether or not it is essential to model acceleration explicitly for sound production in a given ECNI run, a series of numerical simulations were executed to record the upstream acoustic response due to entropy-patch-coked-nozzle interaction. Entropy patches with a dimensionless streamwise length scales  $L_s/S_2 \in \{0.15, 0.3, 0.6, 1.5, 3.0, 4.5, 6.0, 7.5, 9.0, 12.0\}$  were considered, where  $L_s$  is the radius  $R_s$  for spots and half-width  $W_s$  for blocks. The results analyzed in this subsection were generated using the same maximum generation amplitude  $A_{max} =$

$0.03 \text{ W} \cdot \text{m}^{-3}$ . We note that the effect of amplitude was investigated as well; the results of that study are discussed in §2.5.3.

In Fig. 2.8, the scaled maximum upstream acoustic response obtained from numerical simulations is plotted as a function of the dimensionless streamwise length scale of the patch  $L_s/S_2$ , where  $S_2$  is half the nozzle-throat height. In black (filled squares/circles): the maximum upstream acoustic response  $p'_{\max}$  scaled by  $p'_{\text{inertial}}$  (left-hand vertical axis). In red (unfilled squares/circles): the maximum upstream acoustic response  $p'_{\max}$  scaled by  $p'_{\text{matching}}$  (right-hand vertical axis). Entropy spots and blocks are represented as circles and squares respectively.

Two modeling regimes can be identified in Fig. 2.8; viz., the inertial-modeling regime for  $L_s/S_2 \leq 1$  and the matching-condition modeling regime for  $L_s/S_2 > 1$ . Indeed, asymptotic behavior is observed in both cases.

That said, in the case of the matching-condition model entropy blocks compared to entropy spots seem, generally speaking, to be better captured by the model. Conversely, in the case of the inertial model entropy spots seem to have a better representation by the model. We conjecture that in the case of the matching-condition model this is due to the reduction of the domain to a 1-D line, hence variations in geometry are not captured. For the inertial model it is hypothesized that this difference is due to an entropy patch being considered a **point particle** during the derivation (Eq. 2.29), for which entropy spots are a better representation.

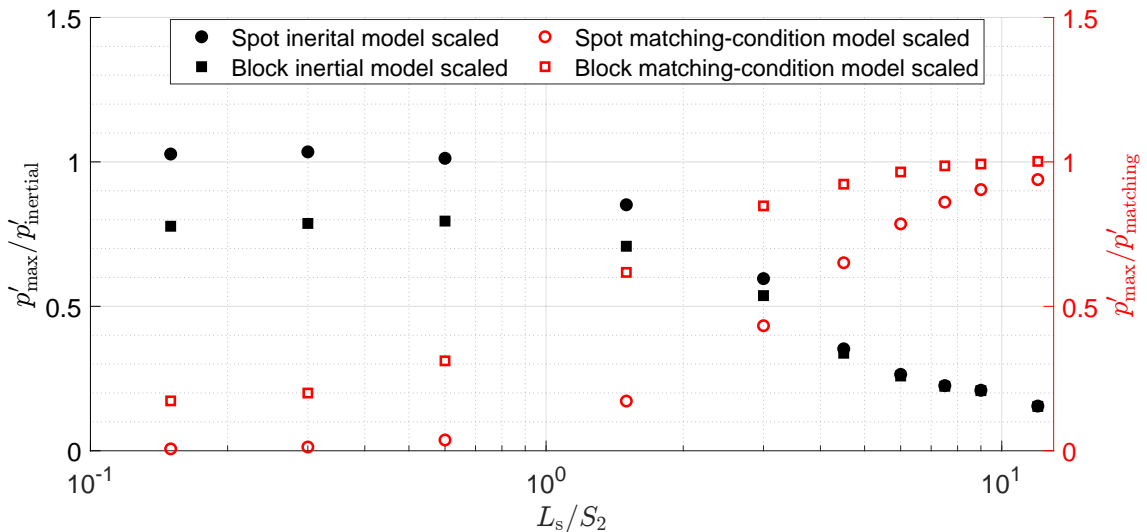


FIGURE 2.8: The maximum upstream acoustic response due to entropy-patch choked nozzle interaction obtained from numerical simulations  $p'_{\max}$  scaled by the inertial model  $p'_{\text{inertial}}$  (left axis) and the matching condition model  $p'_{\text{matching}}$  (right axis) as a function of dimensionless streamwise length scale  $L_s/S_2$ , where  $L_s = R_s$  for entropy spots and  $L_s = W_s$  for entropy blocks.

These results confirm the preliminary results presented by Kowalski et al. [30] with regard to the existence of two distinct modeling regimes; viz., a matching condition modeling regime and an inertial modeling regime. Moreover, the blended-effects regime, where both matching conditions and inertial effects play a role in the production of an upstream acoustic, posited by Kowalski et al. [30] remains a viable

hypothesis.

However, here we identified and demonstrated, for the first time, that  $L_s/S_2$  is an apt dimensionless order parameter. Indeed,  $L_s/S_2$  indubitably allows one to identify by their asymptotes the two matching and inertial regimes. Moreover, this order parameter points to the fact that the size of the entropy patch relative to the throat height is the dominant feature in determining which modeling regime is applicable. E.g., one can confidently assert that for  $L_s/S_2 \geq 1$ , in which case the entropy patch fully occupies the nozzle throat and thus fully changes the thermodynamic state of in nozzle throat: quasi-steady matching condition modeling applies. Whereas, if the entropy patch does not fully occupy the nozzle throat and the force exerted by the walls of the nozzle due to the acceleration of an entropy patch dominates, one falls under the inertial modeling regime. i.e.,  $L_s/S_2$  allows one to unambiguously identify these two fundamentally different sound production mechanisms.

We note that both modeling regimes rely on linearization. I.e., there is a caveat: the above holds provided non-linear effects can be neglected. In the following subsection, we establish the limits of linearization as a viable modeling strategy by means of a relevant dimensionless order parameter dubbed the entropy-patch strength.

### 2.5.3 Determining limits of linearized modeling: Effect of entropy-patch strength on upstream acoustic response prediction by reduced-order models

To investigate linearization as a viable modeling strategy, a series of numerical simulations were performed using entropy patches with different strengths  $e'_e/e_u$ , where  $e_u$  is the area-specific total energy of the upstream channel defined as

$$e_u \equiv \rho_u \left( c_v T_u + \frac{1}{2} u_u^2 \right) \quad (2.39)$$

and  $e'_e$  is the area-specific perturbation energy of the entropy patch. We note that entropy patches are generated using energy injection at a (moving) point into the main flow. This allows one to define  $e'_e$  as the total energy injected during entropy-patch generation scaled by the area of the entropy patch:

$$e'_e = \frac{1}{A_e} \iint Q_E(\zeta, t) dA dt. \quad (2.40)$$

With that in mind, two sets of six ECNI runs were executed respectively in the inertial modeling regime with  $L_s/S_2 = 0.3$  and matching condition modeling regime with  $L_s/S_2 = 9.0$ . Entropy blocks were used given that the shape of the entropy patch has a negligible effect on the applicable modeling regime. For each regime simulations were carried out with  $e'_e/e_u \in \{0.07, 0.30, 3.00, 14.95, 29.90, 89.71\}$ .

The results of these sets of simulations are shown in Fig. 3.1. In Fig. 2.9(a)  $p'_{\max}$  for  $L_s/S_2 \leq 1$  (inertial modeling regime) are scaled by  $p'_{\text{inertial}}$  and in Fig. 2.9(b)  $p'_{\max}$  obtained for  $L_s/S_2 > 1$  (matching condition modeling regime) by  $p'_{\text{matching}}$ . One clearly sees that in both cases for  $e'_e/e_u \lesssim 1$  a horizontal asymptote is found. One deduces that for  $e'_e/e_u \lesssim 1$  linearization is an apt modeling strategy.

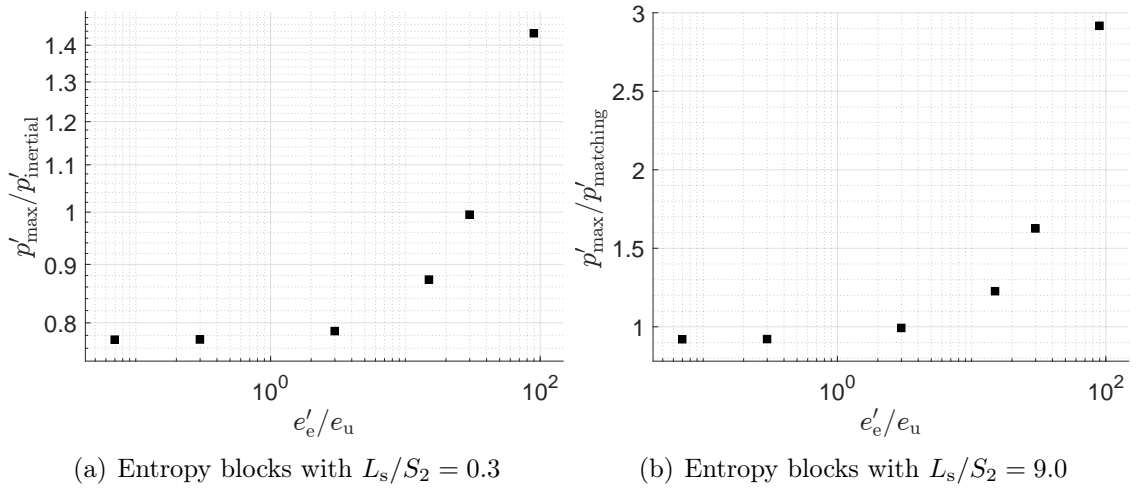


FIGURE 2.9: The maximum upstream acoustic response due to entropy-patch choked nozzle interaction obtained from numerical simulations  $p'_{\max}$  scaled by the inertial model  $p'_{\text{inertial}}$  (Fig. 2.9(a)) and the matching condition model  $p'_{\text{matching}}$  (Fig. 2.9(b)) as a function of the ratio of area-specific perturbation energy of the entropy patch to the area-specific total energy of the upstream channel  $e'_e/e_u$ .

Furthermore, in both cases the scaled acoustic response approaches a vertical asymptote at  $e'_e/e_u \approx 10^2$ . This vertical asymptote is due to the fact that a physical limit of the system is reached; viz., where one approaches an entropy patch with zero density. One can show this by rewriting  $e'_e/e_u$  in terms of the upstream density and the entropy-patch density perturbation as follows (for a detailed derivation refer to Appendix A.6):

$$\frac{e'_e}{e_u} = \left[ \frac{2}{\gamma(\gamma - 1)M_u^2} + 1 \right] \frac{\rho'_e}{\rho_u} \quad (2.41)$$

Given that our system has an upstream Mach number of  $M_u \approx 0.2$  and a specific heat ratio  $\gamma = 1.4$  one finds  $e'_e/e_u \approx 90 \rho'_e/\rho_u$ . With that in mind, one notes that  $e'_e/e_u \approx 90$  is possible when the  $\rho'_e/\rho_u = \rho_e/\rho_u - 1 = 1$ . However, in our ECNI runs  $\rho'_e < 0$ . Thus,  $\rho_e$  would have to be zero which is not possible.

These results show that both the matching condition model and the inertial model are only valid for weak entropy patches  $e'_e/e_u \lesssim 1$ . We note that both models rely on linearization as an essential modeling ingredient. I.e., for  $e'_e/e_u \lesssim 1$  we are in what we will call a linear-modeling regime. Here we have ineluctably demonstrated that there are clear limits to the pertinent use of linear modeling. Indeed, for strong patches  $e'_e/e_u > 1$  neither linear model provides adequate scaling, to wit, nonlinearity is essential.

## 2.6 Conclusion

A systematic numerical simulation study of entropy-patch choked-nozzle interaction was carried out. The results were analyzed by considering linear reduced-order

model-based scaling. This has allowed us to unambiguously confirm the existence of two modeling regimes, to wit, the inertial and (quasi-steady) matching-condition modeling regimes. We have established that the dimensionless order parameter that allows one to determine which modeling regime applies is  $L_s/S_2$  (the streamwise length scale divided by half the nozzle throat height). Indeed, our analysis shows that for  $L_s/S_2 \leq 1$  one finds oneself in the inertial modeling regime, where convective acceleration, which is determined by the nozzle shape, is essential to modeling sound production. For  $L_s/S_2 > 1$ , the sound production mechanism is in what we have termed the matching-condition modeling regime, where a quasi-steady modeling approach is apt. Sound is produced by changing the thermodynamic state at the choked-nozzle throat. Moreover, specifics of nozzle shape such as radius of curvature, are irrelevant to the matching-condition model as it only relies on the contraction ratio which determines the upstream Mach number.

Two types of entropy patches were considered: circular spots and rectangular (slug-like) blocks. Our results show that the exact shape of the entropy patch has only a marginal effect on the applicable modeling regime needed to study the acoustic response due to entropy-patch choked-nozzle interaction.

We have, in addition, established, by means of a dimensionless order parameter, which we call the entropy-patch strength  $e'_e/e_u$ , that there are clear limits to the applicability of linearization as a modeling strategy. Indeed, we determined that for  $e'_e/e_u > 1$  nonlinearity is essential for the description of entropy noise.

# Chapter 3

## Entropy-patch choked-nozzle interaction: Effects of nozzle convergent geometry on scaled upstream acoustic response

### 3.1 Introduction

In Chapter 2 we established the modeling regimes and limits of linearization based on patch characteristics, this chapter focuses on elucidating the role of the nozzle's convergent geometry on sound production.

In particular, we systematically investigate the influence of key geometric parameters of the nozzle inlet. Using EIA, we quantify how variations in nozzle convergent geometry affect the observed upstream acoustic response. The simulation results are scaled and interpreted using the reduced-order models introduced previously, namely, the matching-condition and inertial models, allowing for an assessment of their predictive accuracy across different nozzle configurations.

By doing so, this chapter advances our understanding of how nozzle design influences entropy noise generation mechanisms. These insights are essential for the development of effective noise-mitigation strategies in modern combustion systems, where nozzle geometry can be optimized not only for performance but also for acoustic behavior.

### 3.2 General approach

To investigate the influence of a nozzle's convergent geometry on the scaled upstream acoustic response, numerical simulations were conducted using the EIA [32]. The pressure pulsations arising from the interaction between entropy patches and the choked nozzle were extracted from the simulations and subsequently scaled using two reduced-order models: the matching-condition model and the inertial model, as detailed in §2.3.

The computational domain employed in these simulations is consistent with that

described in §2.2, comprising a nozzle with a throat height of  $2S_2$  and a depth of  $2S_1$ , connected to an upstream chamber with both height and depth equal to  $2S_1$ .

### 3.3 Computational procedure

The computational procedure follows the general approach detailed in §2.4, with minor modifications to accommodate changes in the convergent nozzle geometry. Despite these modifications, the procedure still adheres to the following three-step process:

1. Generation of a computational mesh.
2. Establishment of a steady choked-nozzle base flow.
3. Execution of unsteady entropy-patch–choked-nozzle interaction (ECNI) simulations.

#### 3.3.1 Mesh Generation

This section outlines the mesh generation process for the convergent-divergent nozzle configurations used in the present study.

The numerical domain employs the same multi-block configuration as described previously (see Figure 2.4). The upstream channel is defined by Block B3, with a height of  $S_1 = 1$  m, where entropy patches are generated and convected downstream. Block B2 serves as a transition zone to reduce cell stretching and skewness as it connects to Block B1, which forms the convergent section of the nozzle (i.e., the nozzle inlet). Downstream of the convergent section, Block B4 functions as the diffuser.

For the present study, meshes were generated using a base resolution of 30 points per entropy patch length scale. This resolution ensures a total discretization error of 2.2%, with an observed order of accuracy of 1.9, measured at a distance of  $42R_s/W_s$  from the nozzle inlet (see Appendix B.1).

The primary modification in mesh generation concerns the geometry of Block B1. In the previous configuration (§2.4.1), the nozzle convergent geometry was fixed with a contraction ratio  $C_r = S_1/S_2 = 3$  and a length ratio  $L_r = L_c/S_1 = 1/2$ , where the profile was defined using a Henrici transform [41], as implemented by Hirschberg [34].

In this study, the nozzle convergent geometry was instead defined using a polynomial function to explore its influence on the upstream acoustic response resulting from entropy-patch choked-nozzle interactions. The convergent profile is given by:

$$\frac{S(x)}{S_1} = \frac{1}{C_r} + \left(1 - \frac{1}{C_r}\right) \left(1 - \frac{x}{L_r S_1}\right)^N \quad (3.1)$$

As shown in Equation (3.1), given that the upstream channel height remains constant at  $S_1$ . The shape of the convergent section is governed by three parameters: the contraction ratio  $C_r$ , the length ratio  $L_r$ , and the profile degree  $N$ .

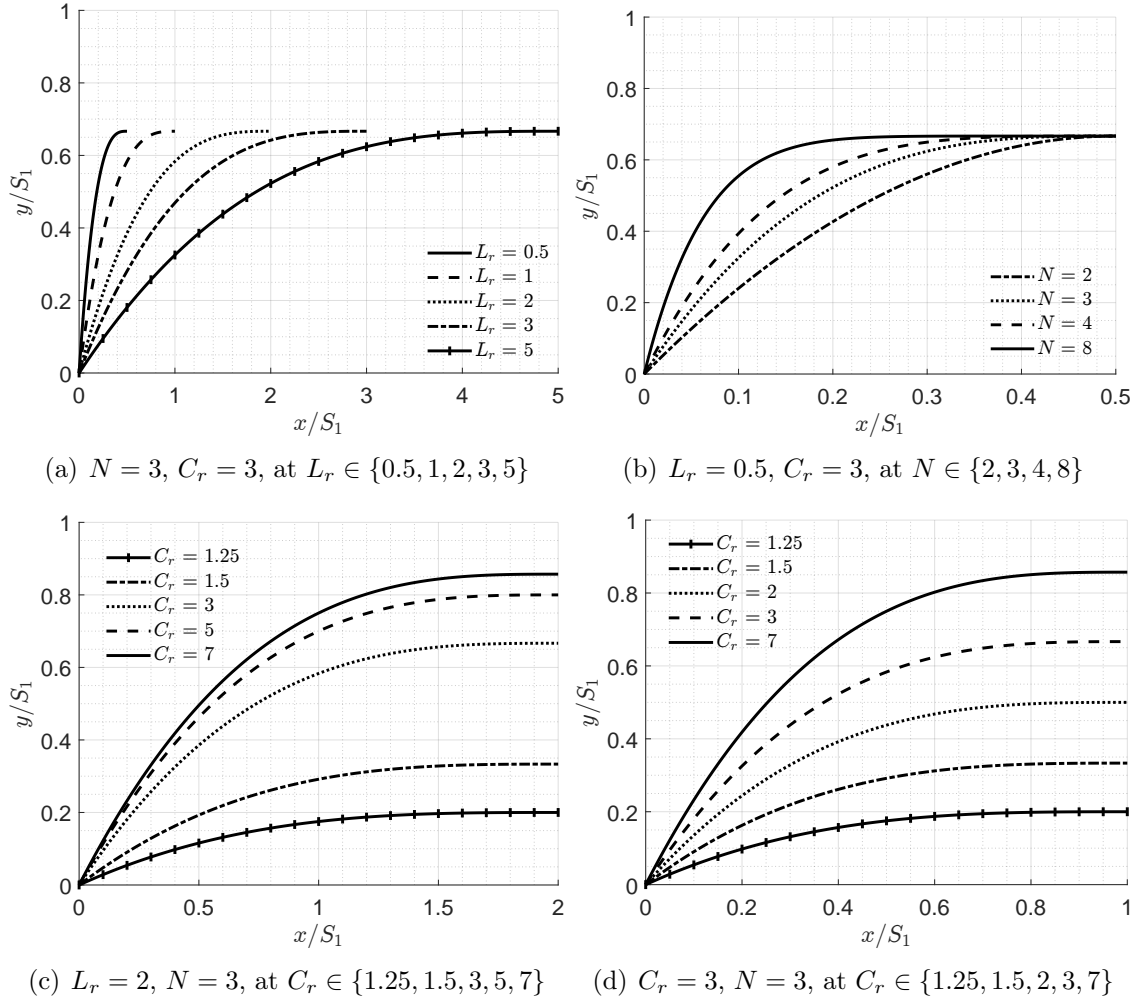


FIGURE 3.1: Nozzle convergent profiles used for investigating the effects of nozzle parameters on the upstream acoustic response due to entropy-patch choked-nozzle interaction.

To examine the effect of each parameter on the upstream acoustic response, a parametric study was conducted in which one parameter was varied while the others were held constant:

- The effect of length ratio was investigated using geometries with  $L_r \in \{0.5, 1, 2, 3, 5\}$  at fixed  $C_r = 3$  and  $N = 3$  (see Figure 3.1(a)).
- The effect of the profile degree was studied using  $N \in \{2, 3, 4, 8\}$  at  $C_r = 3$  and  $L_r = 0.5$  (see Figure 3.1(b)).
- The effect of contraction ratio was assessed with:
  - $C_r \in \{1.25, 1.5, 3, 5, 7\}$  at  $L_r = 2$  and  $N = 3$  (see Figure 3.1(c)).
  - $C_r \in \{1.25, 1.5, 2, 3, 7\}$  at  $L_r = 1$  and  $N = 3$  (see Figure 3.1(d)).

### 3.3.2 Establishing choked-nozzle base flow

The choked-nozzle base flow, which is used to initialize the flow field for the unsteady ECNI simulation, is established as described in §2.4.2. As outlined previously, an initial condition run is performed to establish a choked-nozzle flow, followed by an intermediate run to homogenize the flow field and ensure that transients from the changing boundary conditions between the initial condition run and the ECNI run are dissipated.

It is important to note that in this chapter, we are working with nozzle geometries that have varying contraction ratios. Therefore, the initial condition for the upstream blocks and the inflow boundary condition at the upstream boundaries must be adjusted to set the appropriate velocity required to achieve a choked-nozzle flow  $U_{\text{des}}$ . The  $U_{\text{des}}$  values required to achieve choked-nozzle flow for  $C_r \in \{1.25, 1.5, 2, 3, 5, 7\}$  are  $U_{\text{des}} \in \{0.46, 0.39, 0.29, 0.19, 0.12, 0.08\} \text{ m} \cdot \text{s}^{-1}$ , respectively (see Appendix A.5).

The discretization methods used are consistent with those described earlier. Both the initial condition and intermediate runs employ a Roe-TVD scheme with a Van Leer limiter for spatial discretization. Temporal discretization is performed using a second-order accurate, four-stage (4,2) Runge-Kutta scheme with alpha coefficients of (0.240, 0.375, 0.5, 1.0), and a maximum Courant limit of 1.0. Artificial dissipation is applied during the first stage. Time marching is carried out using a non-time-accurate method, as the focus is on obtaining the steady-state solution.

### 3.3.3 Entropy-patch choked-nozzle interaction simulations

For the ECNI runs, the same procedure is followed as outlined in §2.4.3. However, special attention must be given to the generation of entropy patches.

In this study, entropy blocks with a streamwise length scale  $L_s \in \{0.2, 4.0\} \text{ m}$  are used for the nozzle length ratio study (§3.4.1) and nozzle degree study (§3.4.2), corresponding to a dimensionless streamwise length scale of  $L_s/S_2 \in \{0.6, 12\}$ , respectively. For the nozzle contraction ratio study (§3.4.3), entropy blocks with a streamwise length scale  $L_s \in \{0.2, 4.0\} \text{ m}$  are also used. Specifically, entropy blocks with  $L_s = 0.2 \text{ m}$  were used for nozzle configurations with  $C_r \in \{1.25, 1.5, 3, 5, 7\}$ , resulting in  $L_s/S_2 \in \{0.25, 0.3, 0.6, 1, 1.4\}$ . Entropy blocks with  $L_s = 4.0 \text{ m}$  were used for nozzle configurations with  $C_r \in \{1.25, 1.5, 2, 3, 7\}$ , corresponding to  $L_s/S_2 \in \{5.0, 6.0, 8.0, 12.0, 28.0\}$ .

For the nozzle-inlet length ratio study (§3.4.1) and nozzle degree study (§3.4.2), entropy blocks were generated with  $\tau_{\text{start}} = \tau_{\text{end}} = 6 \text{ s}$  and  $\tau_{\text{max}} = 3 \text{ s}$  at  $A_{\text{max}} = 0.03 \text{ W} \cdot \text{m}^{-3}$ . For the nozzle contraction ratio study (§3.4.3), some of the entropy blocks with  $L_s = 4.0 \text{ m}$  were generated with different time scales. This was necessary as the blocks convected with the flow at different velocities, which are dependent on the contraction ratio. These adjustments ensured that all entropy blocks were fully mature as they approached the nozzle inlet.

Additionally, for the nozzle contraction ratio study (§3.4.3), it is important to note that using the same entropy generation profile for runs with varying contraction ratios would result in entropy blocks with different relative excess density/excess mass. This is due to the flow field of the intermediate run converging to different

$L_s$ [m]	$C_r$ [-]	$A_{\max}$ [W · m <sup>-3</sup> ]	$\tau_{\text{start}}$ [s]	$\tau_{\text{max}}$ [s]	$\tau_{\text{end}}$ [s]
0.2	1.25	4.20e-3	6.0	3.0	6.0
	1.50	4.09e-3	6.0	3.0	6.0
	3.00	4.00e-3	6.0	3.0	6.0
	5.00	3.99e-3	6.0	3.0	6.0
	7.00	3.98e-3	6.0	3.0	6.0
4.0	1.25	4.65e-3	1.0	2.0	1.0
	1.50	2.15e-3	3.5	3.0	3.5
	2.00	1.64e-3	5.0	3.5	5.0
	3.00	1.55e-3	6.0	3.0	6.0
	7.00	1.54e-3	6.0	3.0	6.0

TABLE 3.1: Entropy block generation settings used for the contraction ratio study (§3.4.3)

equilibria depending on the contraction ratio of the system. Therefore, special care was taken to generate entropy blocks with  $L_s = 4.0$  m that had the same excess density ratio ( $\rho'_e/\rho_u$ ), as these results were scaled using the matching-condition model. Furthermore, entropy blocks with  $L_s = 0.2$  m were generated to have the same excess mass ( $m_e$ ), as their results were scaled using the inertial model.

The settings used to generate entropy patches that fulfill the requirements mentioned above are provided in Table 3.1. For details on how these values were obtained, the reader is referred to §A.7.

## 3.4 Results & discussion

### 3.4.1 Effect of nozzle-inlet length ratio on the upstream acoustic response

In this section, an investigation of the effects of the nozzle’s length ratio on the inertial and matching-condition models predictive quality is carried out. To this end, numerical simulations were performed using nozzles with  $C_r = 3$  and  $N = 3$ , at length ratios  $L_r \in \{0.5, 1, 2, 3, 5\}$ .

From the intermediate runs, the convective acceleration term  $u(du/dx)$  along the nozzle symmetry line was extracted and used as input for the inertial model. The resulting dimensionless upstream acoustic response, defined as  $|p'_u|S_1^3/(m_e U_u^2)$ , is plotted as a function of the dimensionless sound-source location  $(x_s - x_{\text{th}})/L_c$  within the convergent portion of the nozzle for different values of  $L_r$  in Figure 3.2.

As shown in Figure 3.2, nozzles with a lower contraction length ratio  $L_r$  exhibit, overall, higher levels of sound production. This behavior is expected, as the inertial model attributes sound generation to the acceleration of fluid elements through the nozzle. Since all nozzles begin with the same inlet Mach number and reach Mach 1 at the throat, a lower  $L_r$  means the flow must accelerate more rapidly over a shorter distance, resulting in stronger convective acceleration and thus more sound production.

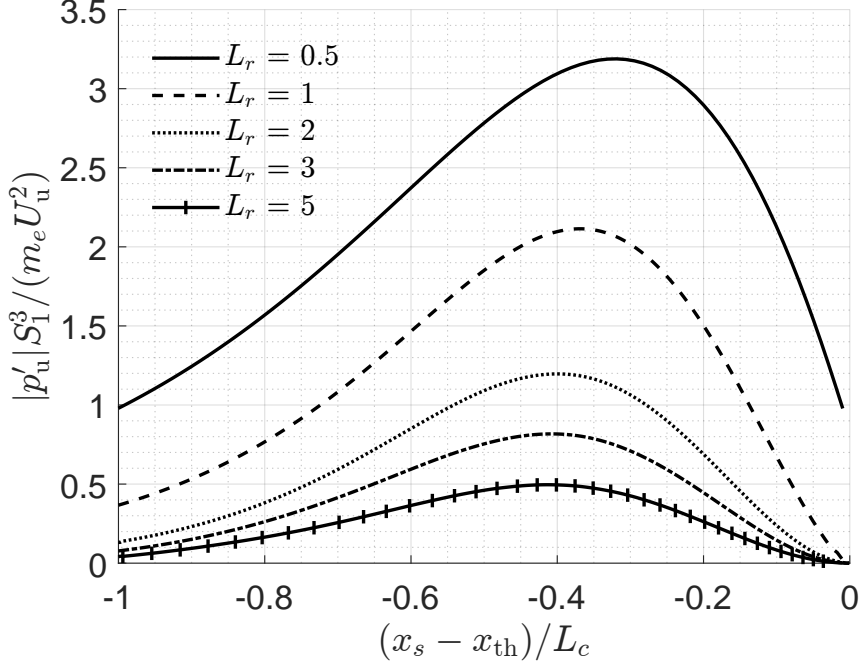


FIGURE 3.2: Dimensionless upstream observed acoustic response  $|p'_u|S_1^3/(m_e U_u^2)$  obtained from the inertial model as a function of the dimensionless source position  $(x_s - x_{th})/L_c$  for nozzles with  $C_r = 3$  and  $N = 3$  for  $L_r \in \{0.5, 1, 2, 3, 5\}$ .

Furthermore, it should be noted that for  $L_r \in \{2, 3, 5\}$  we observe a maxima in the dimensionless upstream acoustic response at  $(x_s - x_{th})/L_c = -0.4$  while for  $L_r \in \{0.5, 1\}$  this maxima shifts to  $(x_s - x_{th})/L_c \in \{-0.32, -0.36\}$ , respectively. It is hypothesized that this shift is due to a rise in the significance of centripetal acceleration. This can be seen by considering the mechanisms of acceleration in the nozzle. The first of which is the acceleration due to the change of the height of the nozzle, which is proportional to the change of height of the nozzle [35, 42]. The second mechanism of acceleration is due to the centripetal acceleration, which is proportional to the height of the nozzle over the radius of curvature of the nozzle profile ( $a_c \sim S/R$ ) [35, 43]. Using this one finds that for nozzles with  $L_r \in \{2, 3, 5\}$  have  $\max(a_c) < 1$  while nozzles with  $L_r \in \{0.5, 1\}$  have  $\max(a_c) > 1$ , showing an increase in significance of the centripetal acceleration.

To check the influence of the nozzle-inlet length ratio on the predictive quality of the inertial model, blocks with  $L_s/S_2 = 0.6$  were used to run entropy-patch choked-nozzle simulations. The recorded upstream pressure response obtained from EIA was scaled using the maximum of the predicted acoustic response as previously discussed in §2.5.1. The results can be seen in Figure 3.3, the maximum upstream acoustic response obtained from numerical simulations  $p'_{\max}$  scaled by the inertial model  $p'_{\text{inertial}}$  is plotted as a function of the dimensionless streamwise length scale of the patch  $10L_s/L_c$ , where  $L_c$  is the length of the nozzle convergent.

As can be seen in Figure 3.3, one observes asymptotic behavior for  $10L_s/L_c < 1$ , or more generally, when  $L_s/L_c \ll 1$ . This brings into light a new dimensionless parameter that strongly influences the predictive quality of the inertial model. Not only is the streamwise length scale of the entropy patch relative to the height of the

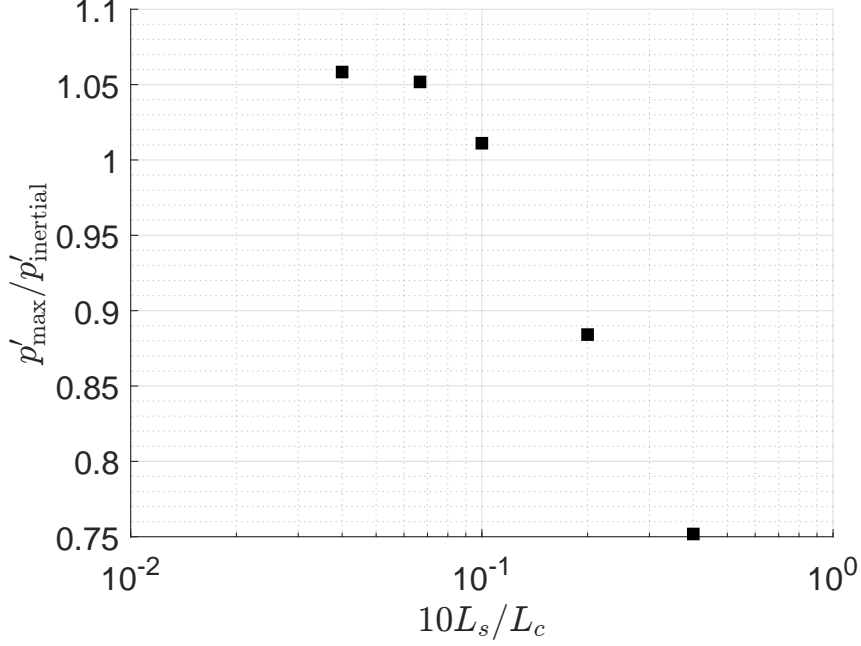


FIGURE 3.3: The maximum upstream acoustic response due to entropy-patch choked nozzle interaction obtained from numerical simulations  $p'_{\max}$  scaled by the inertial model  $p'_{\text{inertial}}$  as a function of dimensionless length scale  $10L_s/L_c$  for blocks with  $L_s/S_2 = 0.6$

nozzle throat relevant for determining the predictive quality of the inertial model, as discussed in the previous chapter, but also the streamwise length scale of the entropy patch relative to the nozzle contraction length. The effect of the streamwise length scale of the entropy patch relative to the nozzle contraction length on the inertial model can be attributed to two system properties:

1. During the derivation of the inertial model, entropy patches are considered to be **point particles**, which is a good approximation for entropy patches with  $L_s/L_c \ll 1$ .
2. The inertial model is based on quasi-1D theory, in which it is assumed that the rate of change of the nozzle height is considered to be very small [35, 43].

Given that all nozzles in this study have the same contraction ratio with varying length ratios, nozzles with a higher  $L_r$  have a lower rate of change of the nozzle height. The effect of the rate of change of the nozzle height will be further expanded upon in §3.4.2.

To investigate the effect of the nozzle-inlet length ratio on the matching-condition model's predictive quality, blocks with  $L_s/S_2 = 12$  were used to run entropy-patch choked-nozzle simulations. The recorded upstream pressure response obtained from EIA was scaled using the matching-condition model as previously discussed in §2.5.1. The results can be seen in Figure 3.3, the maximum upstream acoustic response obtained from numerical simulations  $p'_{\max}$  scaled by the matching-condition model  $p'_{\text{matching}}$  is plotted as a function of the dimensionless streamwise length scale of the patch ( $L_s/L_c$ ), where  $L_c$  is the length of the nozzle contraction.

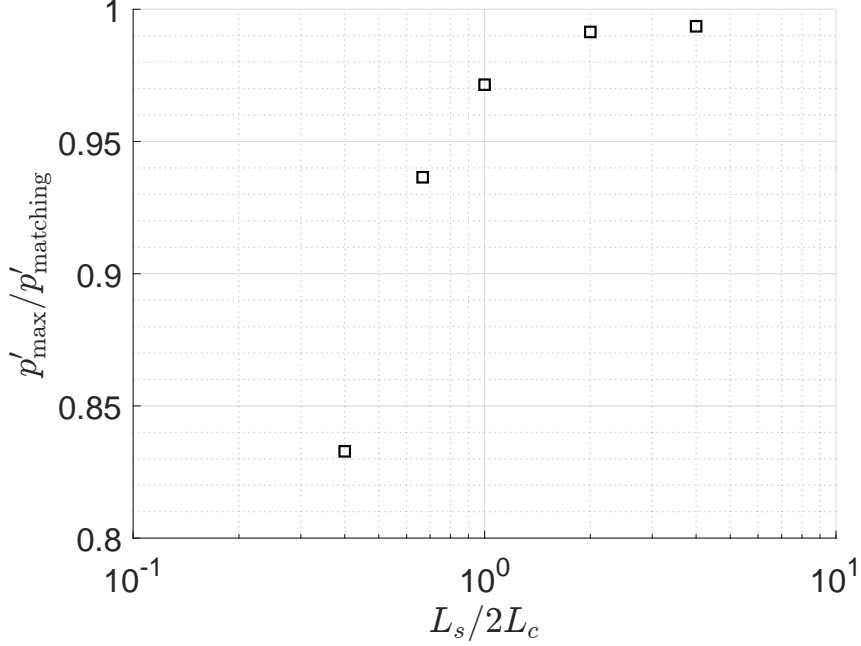


FIGURE 3.4: The maximum upstream acoustic response due to entropy-patch choked nozzle interaction obtained from numerical simulations  $p'_{\max}$  scaled by the matching-condition model  $p'_{\text{matching}}$  as a function of dimensionless length scale  $L_s/2L_c$  for blocks with  $L_s/S_2 = 12$

In contrast to the inertial model, one observes asymptotic behavior for entropy patches with a dimensionless streamwise length scale  $L_s/2L_c > 1$  (in a more general form  $L_s/L_c > 1$ ). This shows that the length scale of the entropy patch relative to the nozzle contraction length is a determining factor for the predictive quality of the matching-condition model, as it is for the inertial model. The relevance of the streamwise length scale of the entropy patch relative to the nozzle contraction length is most probably from the matching condition model, reducing the domain to a 1-D line where the nozzle acts as a discontinuity with a matching condition for the upstream and downstream domains. Given  $L_s/S_2 > 1$  for entropy patches with  $L_s/L_c > 1$ , the nozzle presents itself as a discontinuity relative to the entropy patch.

These findings indicate that for one to fall within the asymptotic region of the inertial modeling regime, the entropy patch must possess not only  $L_s/S_2 < 1$  but also  $L_s/L_c \ll 1$ . Conversely, for one to fall within the asymptotic domain of the matching-condition modeling regime, the entropy patch must possess not only  $L_s/S_2 > 1$  but also  $L_s/L_c > 1$ .

### 3.4.2 Effect of nozzle contraction shape on the upstream acoustic response

In this section, a study of the effect of the nozzle contraction shape on the inertial and matching-condition models' predictive quality is reported. The study was done by running numerical simulations on nozzles with  $N \in \{2, 3, 4, 8\}$  at  $L_r = 0.5$  and

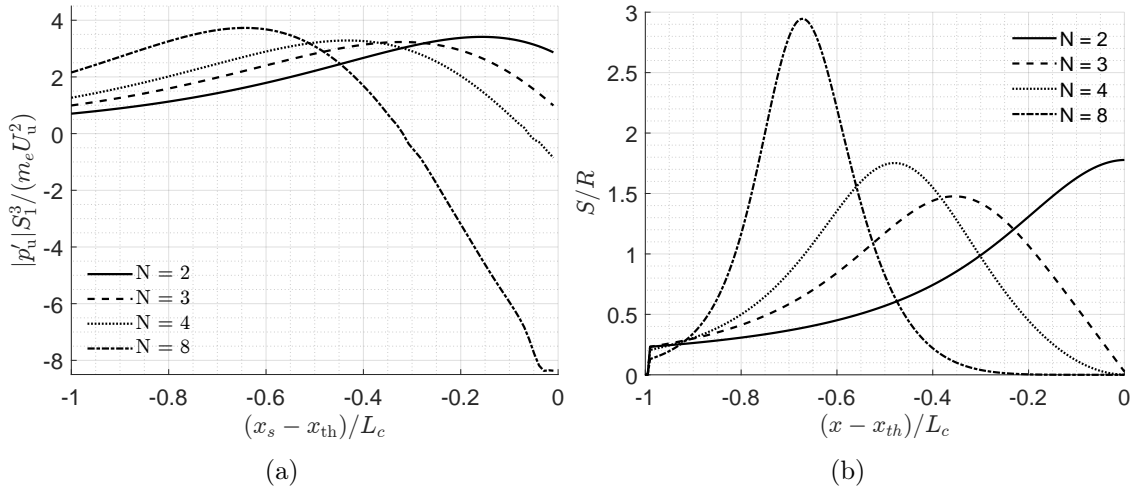


FIGURE 3.5: (a) Dimensionless upstream observed acoustic response  $|p'_u|S_1^3/(m_e U_u^2)$  obtained from the inertial model as a function of the dimensionless source position  $(x_s - x_{th})/L_c$  for nozzles with  $L_r = 0.5$  and  $C_r = 3$  for  $N \in \{2, 3, 4, 8\}$ . (b) Magnitude of centripetal acceleration ( $S/R$ ) as a function of the dimensionless position  $(x - x_{th})/L_c$  for nozzles with  $L_r = 0.5$  and  $C_r = 3$  for  $N \in \{2, 3, 4, 8\}$ .

$C_r = 3$ , where the recorded upstream acoustic response is scaled by the prediction of the inertial model or the matching-condition model, depending on which modeling regime one falls under. The nozzles used for this study can be seen in Figure 3.1(b).

As previously done, the convective acceleration from the intermediate run was used as an input for the inertial model. The dimensionless upstream acoustic response  $|p'_u|S_1^3/(m_e U_u^2)$  as a function of dimensionless sound-source location  $(x_s - x_{th})/L_c$  in the convergent part of the nozzle for varying  $N$  can be seen in Figure 3.5(a). As can be seen in Figure 3.5(a), the maxima of the inertial model move closer to the inlet of the nozzle as  $N$  increases. It is proposed that this change is due to the point of highest centripetal acceleration (hence the smallest radius of curvature) moving closer to the nozzle inlet. This can be seen by taking  $S/R$  (a measure of the centripetal acceleration [35, 43]) along the nozzle convergent profile Figure 3.5(b). Furthermore, it should be noted that the location of maximum sound production given by the inertial model converges to the location of maximum centripetal acceleration for nozzles with a high value for  $N$ , as centripetal acceleration becomes a dominant acceleration mechanism.

To check the effect of the nozzle shape on the inertial model's predictive quality, entropy blocks with  $L_s/S_2 = 0.6$  and  $10L_s/L_c = 3$  were used to run entropy-patch choked-nozzle simulations. The recorded upstream pressure response obtained from EIA was scaled using the maximum of the predicted acoustic response provided by the inertial model, as previously done. The results can be seen in Figure 3.6 where the maximum upstream acoustic response due to entropy-patch choked-nozzle interaction obtained from numerical simulations  $p'_{\max}$  scaled by the inertial model  $p'_{\text{inertial}}$  is plotted as a function of the quasi-1D parameter  $\max(\frac{S}{R} \frac{dS}{dx})$ . Data points with a higher  $\max(\frac{S}{R} \frac{dS}{dx})$  correlate to a higher  $N$ .

As can be seen in Figure 3.6, the inertial model provides a better prediction

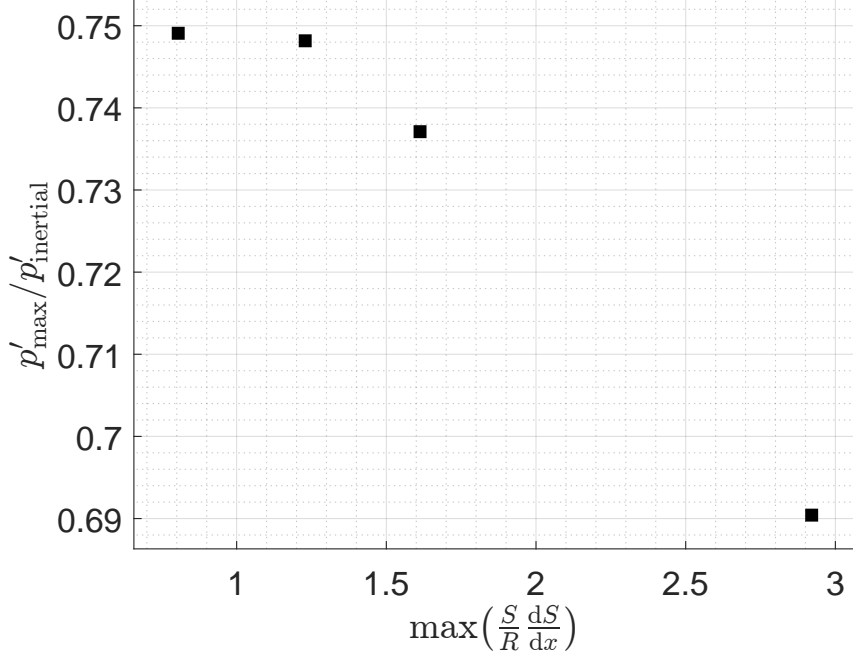


FIGURE 3.6: The maximum upstream acoustic response due to entropy-patch choked-nozzle interaction obtained from numerical simulations  $p'_{\max}$  scaled by the inertial model  $p'_{\text{inertial}}$  as a function of the quasi-1D parameter  $\max\left(\frac{S}{R} \frac{dS}{dx}\right)$  for blocks with  $L_s/S_2 = 0.6$  and  $10L_s/L_c = 3$

for nozzle convergent profiles with a lower  $\max\left(\frac{S}{R} \frac{dS}{dx}\right)$ . Moreover, it can be seen that asymptotic behavior is observed for  $\max\left(\frac{S}{R} \frac{dS}{dx}\right) \leq 1$ . This is expected as the derivation of the inertial model assumes a quasi-1D flow profile for the nozzle. A quasi-1D flow profile refers to a flow configuration where flow variables vary primarily along one spatial direction. Both Thompson and Crocco state that for the quasi-1D condition to be met, the nozzle profile must satisfy two conditions:  $S/R \ll 1$  and  $dS/dx \ll 1$  [35, 43]. However, as can be seen in Figure 3.6, in the case of the inertial modeling regime that there is an interplay between both conditions. Meaning that if one of the conditions is of order one and the other of an order of magnitude less, one can still apply quasi-1D flow approximations.

To check the effect of the nozzle convergent shape on the matching-condition model's predictive quality, entropy blocks with  $L_s/S_2 = 12$  and  $L_s/2L_c = 4$  were used to run the entropy-patch choked-nozzle simulations. The recorded upstream pressure response obtained from EIA was scaled using the matching-condition model. The results can be seen in Figure 3.7, where the maximum upstream acoustic response due to entropy-patch choked-nozzle interaction obtained from numerical simulations  $p'_{\max}$  scaled by the matching-condition model  $p'_{\text{matching}}$  is plotted as a function of the quasi-1D parameter  $\max\left(\frac{S}{R} \frac{dS}{dx}\right)$ . The results show that as the quasi-1D decreases, the predictive accuracy of the matching-condition model increases. Conversely, it seems that one approaches an asymptote for  $\max\left(\frac{S}{R} \frac{dS}{dx}\right) > 1$  which would make sense as the matching condition model assumes a 1D domain where the nozzle is a discontinuity. It should be realized that the numerical results have a 2% error, meaning all of the data points fall within the same error range.

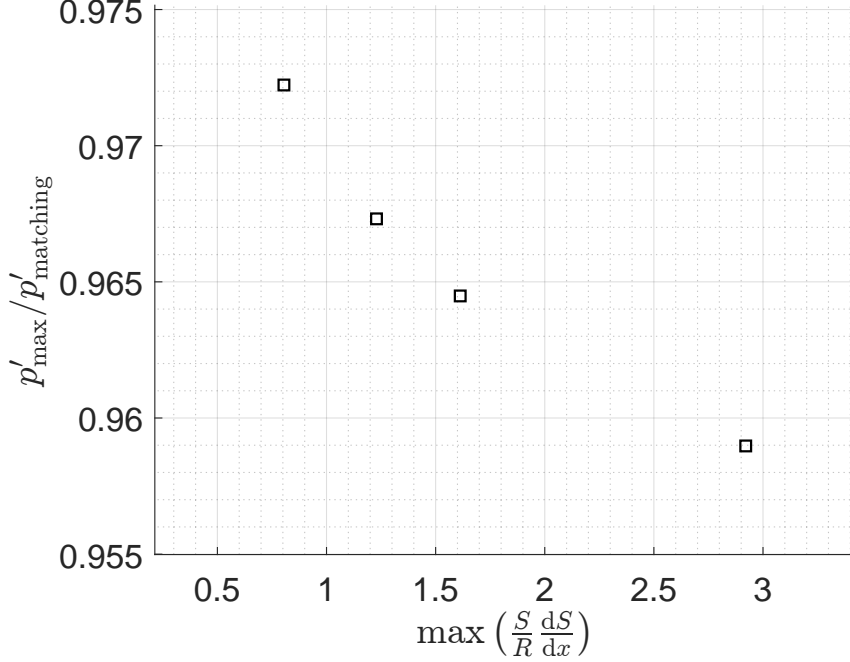


FIGURE 3.7: The maximum upstream acoustic response due to entropy-patch choked-nozzle interaction obtained from numerical simulations  $p'_{\max}$  scaled by the matching-condition model  $p'_{\text{matching}}$  as a function of the quasi-1D parameter  $\max(\frac{S}{R} \frac{dS}{dx})$  for blocks with  $L_s/S_2 = 12$  and  $L_s/2L_c = 4$

These results show that, given an entropy patch in the matching-condition regime ( $L_s/S_2 > 1$  and  $L_s/L_c > 1$ ), the shape of the nozzle convergent has negligible to no effect on the predictive quality of the matching-condition modeling approach for the prediction of the upstream acoustic response due to entropy-patch choked-nozzle interaction. However, for the inertial model, it seems that profiles with a quasi-1D profile ( $\max(\frac{S}{R} \frac{dS}{dx}) < 1$ ) yield a better result.

### 3.4.3 Effect of nozzle contraction ratio on the upstream acoustic response

In this section, the effect of the contraction ratio on the inertial and the matching-condition models predictive quality is investigated. For the inertial modeling regime, computations were run using nozzle convergent geometries with  $L_r = 2$  and  $N = 3$  for  $C_r \in \{1.25, 1.5, 3, 5, 7\}$ .

The convective acceleration from the intermediate run was used as an input for the inertial model. The dimensionless upstream acoustic response  $|p'_u|S_1^3/(m_e U_u^2)$  as a function of dimensionless sound-source location  $(x_s - x_{\text{th}})/L_c$  in the convergent part of the nozzle for varying  $N$  can be seen in Figure 3.8. As can be seen in Figure 3.8, as the contraction ratio of the nozzle increases, the maximum dimensionless upstream acoustic response increases exponentially, and the location of that maxima moves closer to the nozzle throat. The global increase of the dimensionless upstream acoustic response can be attributed to the Mach profile of the nozzle convergent. As can be seen in Figure 3.9(a), nozzles with a higher contraction ratio have a lower

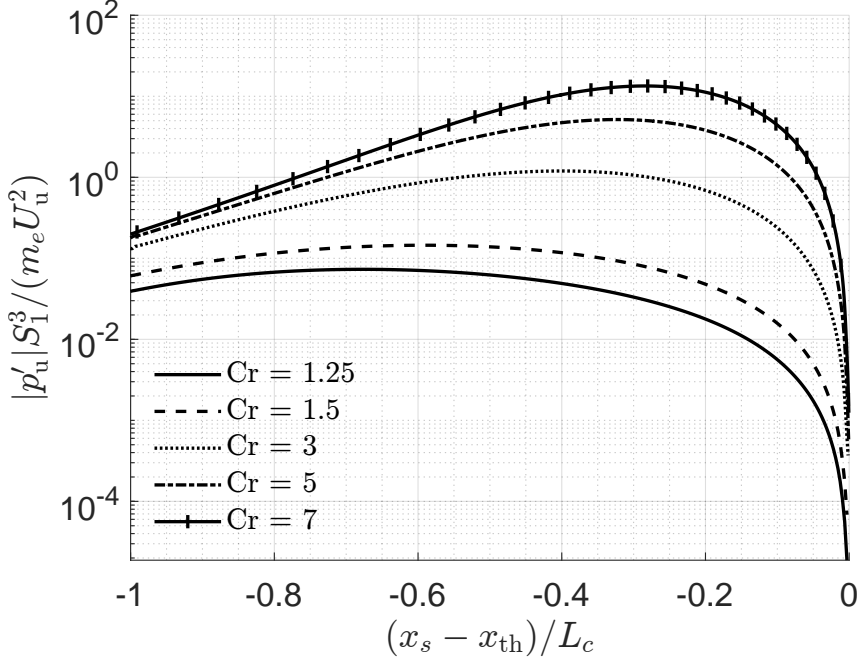


FIGURE 3.8: Dimensionless upstream observed acoustic response  $|p'_u| S_1^3 / (m_e U_u^2)$  obtained from the inertial model as a function of the dimensionless source position  $(x_s - x_{th}) / L_c$  for nozzles with  $L_r = 3$  and  $N = 3$  at  $C_r \in \{1.25, 1.5, 3, 5, 7\}$ .

upstream Mach number, which is expected as one is dealing with choked nozzle flow (Appendix A.5). Now consider the inertial model (Equation (2.30)), if one takes the Mach number at the sound source ( $M_s$ ) to be constant, the observed upstream acoustic response increases as the upstream Mach number decreases, which is the case for nozzles with higher contraction ratios. As for the shift of the maxima of the observed upstream acoustic response closer to the nozzle throat, as well as the local increase of the maxima, can be attributed to the increase of the convective acceleration. As can be seen in Figure 3.9(b) as the contraction ratio of the nozzle increases, the maxima of the convective acceleration moves closer to the nozzle throat. Moreover, the magnitude of the maxima increases as the contraction ratio increases.

Entropy-patch choked-nozzle simulations were performed using entropy blocks with a dimensionless streamwise length-scale  $10L_s/L_c = 1$ . The recorded upstream pressure response obtained from EIA was scaled using the inertial model. The results can be seen in Figure 3.10, where the maximum upstream acoustic response due to entropy-patch choked-nozzle interaction obtained from numerical simulations  $p'_{\max}$  scaled by the inertial model  $p'_{\text{inertial}}$  is plotted as a function of the dimensionless streamwise length-scale  $L_s/S_2$ . It can be seen that as  $L_s/S_2$  decreases, the scaled acoustic response increases at an exponential rate. This shows a clear trend where the inertial model underpredicts the magnitude of the acoustic response for small entropy patches, which was not the case in the previous study in chapter 1. This can only be attributed to the change of the upstream Mach number<sup>1</sup>. Note that the

<sup>1</sup>All entropy blocks were generated to have  $e'_e/e_u < 1$  to ensure one falls under the linear modeling regime

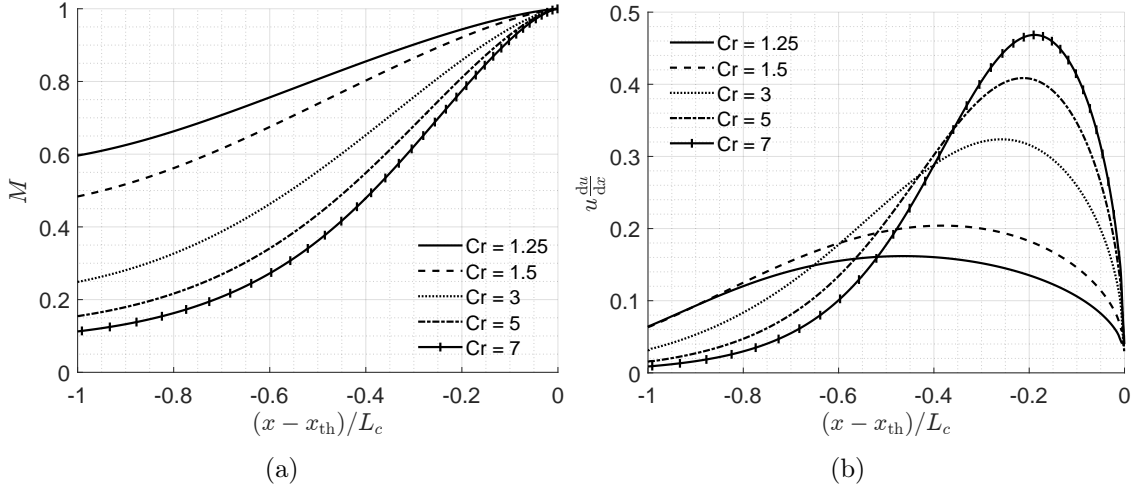


FIGURE 3.9: (a) Mach number as a function of the dimensionless position  $(x - x_{th})/L_c$  for nozzles with  $L_r = 2$  and  $N = 3$  at  $C_r \in \{1.25, 1.5, 3, 5, 7\}$ . (b) Convective acceleration ( $u(du/dx)$ ) as a function of the dimensionless position  $(x - x_{th})/L_c$  for nozzles with  $L_r = 2$  and  $N = 3$  for  $C_r \in \{1.25, 1.5, 3, 5, 7\}$ .

dimensionless streamwise length-scale is varied by changing the contraction ratio hence,  $L_s/S_2 \in \{0.25, 0.3, 0.6, 1, 1.4\}$  correspond to upstream Mach numbers  $M_u \in \{0.55, 0.43, 0.20, 0.12, 0.08\}$  respectively. This brings into light the significance of the upstream Mach number as entropy blocks that were previously in the asymptotic range of the inertial modeling regime are no longer well predicted by the inertial model.

For the matching-condition modeling regime, computations were run using nozzle convergent geometries with  $L_r = 1$  and  $N = 3$  for  $C_r \in \{1.25, 1.5, 2, 3, 7\}$ . Entropy-patch choked-nozzle simulations were performed using entropy blocks with a dimensionless streamwise length-scale  $L_s/2L_c = 2$ . The recorded upstream pressure response obtained from EIA was scaled using the matching-condition model. The results can be seen in Figure 3.10, where the maximum upstream acoustic response due to entropy-patch choked-nozzle interaction obtained from numerical simulations  $p'_{\max}$  scaled by the matching-condition model  $p'_{\text{matching}}$  is plotted as a function of the dimensionless streamwise length-scale  $L_s/S_2$ . As can be seen in Figure 3.11, as the dimensionless streamwise length-scale  $L_s/S_2$  increases, the scaled pressure response increases and reaches an asymptote at unity. From this, we reach the same conclusion as in chapter 1, where one falls under the asymptotic region of the matching-condition modeling regime for entropy patches with a dimensionless streamwise length-scale  $L_s/S_2 > 1$ . Note that the dimensionless streamwise length-scale was varied by changing the contraction ratio hence,  $L_s/S_2 \in \{5, 6, 8, 12, 28\}$  correspond to upstream Mach numbers  $M_u \in \{0.55, 0.43, 0.29, 0.20, 0.08\}$  respectively.

From these results it is observed that the inertial model fails to accurately predict the acoustic response for entropy patches with dimensionless streamwise length-scale  $L_s/S_2 < 1$ , particularly at  $L_s/S_2 \in \{0.25, 0.3\}$ , which correspond to higher upstream Mach numbers  $M_u \in \{0.55, 0.43\}$ , respectively. This discrepancy suggests

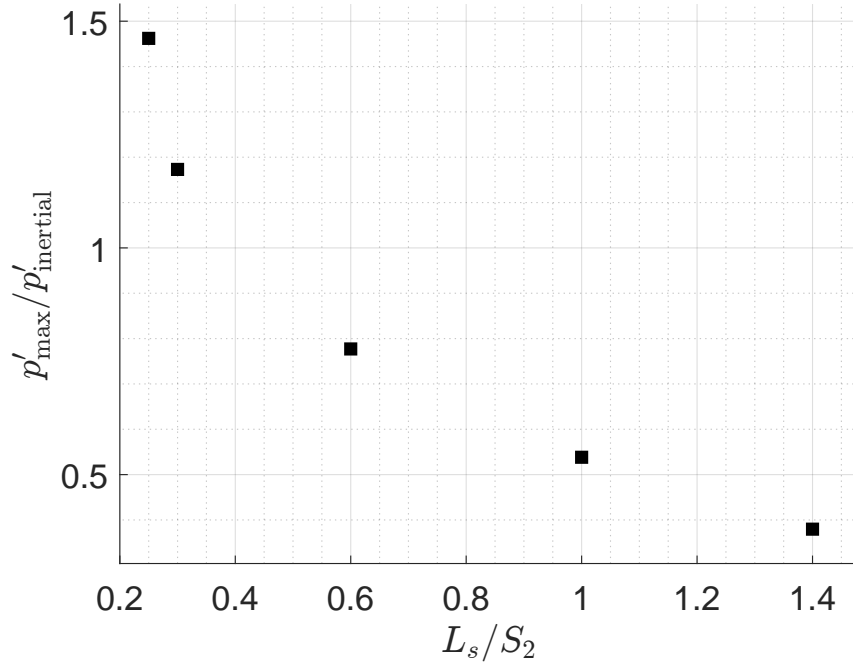


FIGURE 3.10: The maximum upstream acoustic response due to entropy-patch choked-nozzle interaction obtained from numerical simulations  $p'_{\max}$  scaled by the inertial model  $p'_{\text{inertial}}$  as a function of the dimensionless streamwise length-scale  $L_s/S_2$  for blocks with  $10L_s/L_c = 1$

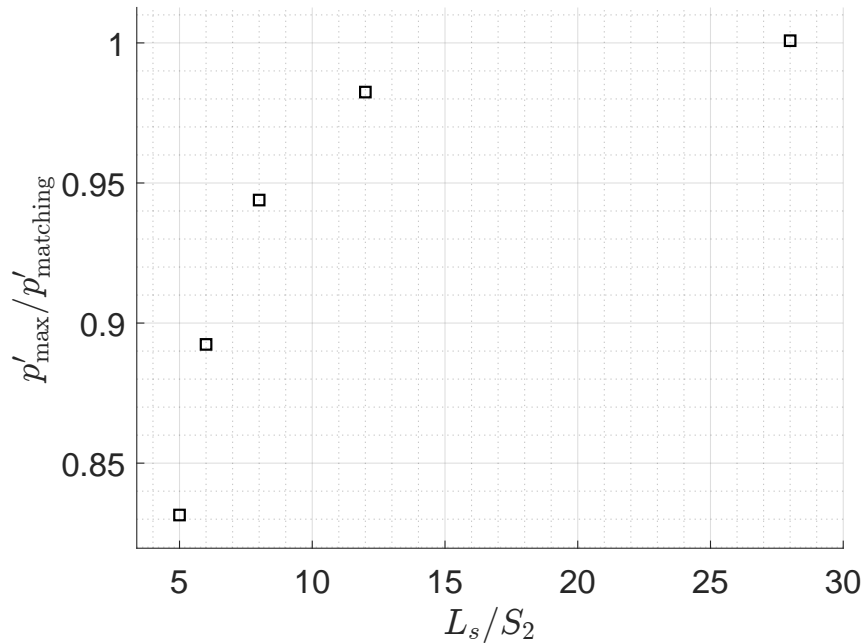


FIGURE 3.11: The maximum upstream acoustic response due to entropy-patch choked-nozzle interaction obtained from numerical simulations  $p'_{\max}$  scaled by the matching-condition model  $p'_{\text{matching}}$  as a function of the dimensionless streamwise length-scale  $L_s/S_2$  for blocks with  $L_s/2L_c = 2$

a limitation of the inertial model under these conditions, likely due to the increasing influence of compressibility effects that are not adequately captured. It is therefore hypothesized that the inertial model loses predictive quality for choked nozzle flows with upstream Mach numbers greater than approximately  $M_u > 0.3$ . In contrast, the matching-condition model is unaffected by high upstream Mach numbers and shows good agreement with numerical results for larger entropy patches ( $L_s/S_2 > 1$ ), where the response asymptotically approaches the model prediction.

### 3.5 Conclusion

This study examined the impact of nozzle geometry on the upstream acoustic response resulting from entropy-patch choked-nozzle interactions, with particular focus on the predictive quality and behavior of the inertial and matching-condition models. The analysis was carried out using both the inertial and matching-condition reduced-order models to scale results from numerical simulations carried out using EIA. Three geometric parameters were investigated:

1.  $L_r$  the nozzle-inlet length ratio.
2.  $N$  what we have called the degree of the nozzle (influences the contraction's shape).
3. The contraction ratio  $C_r$ .

For the contraction length ratio, it was found that as the length of the nozzle inlet decreases (lowering  $L_r$ ), the inertial model produces a stronger acoustic response due to higher convective acceleration, a direct consequence of the need to reach Mach 1 over a shorter distance. Additionally, the location of peak acoustic response shifts depending on the relative significance of centripetal acceleration. The results further revealed that for the inertial model to hold, the streamwise length scale of the entropy patch must not only be small relative to the throat height ( $L_s/S_2 < 1$ ), but also small relative to the nozzle contraction length ( $L_s/L_c \ll 1$ ). Conversely, for the matching-condition model, predictive quality was achieved when the entropy patch length scale was large compared to both the throat height and contraction length ( $L_s/S_2 > 1$ ,  $L_s/L_c > 1$ ), implying that the nozzle behaves effectively as a geometric discontinuity in such cases.

In terms of the contraction shape, results demonstrated that increasing  $N$  (which corresponds to sharper curvature and greater deviation from a quasi-1D profile) causes the location of maximum acoustic response obtained from the inertial model to move upstream. It was deduced that for these sharply curved inlets, centripetal acceleration plays a non-negligible role. The inertial model's predictive accuracy was strongly affected by the degree to which the flow adhered to quasi-1D assumptions. Nozzles with lower values of the quasi-1D parameter  $\max(\frac{S}{R} \frac{dS}{dx})$  showed better agreement with the model predictions, with asymptotic accuracy observed for values below unity. In contrast, the matching-condition model was shown to be largely insensitive to changes in nozzle shape, reaffirming that in this regime the nozzle effectively acts as a one-dimensional discontinuity.

For the contraction ratio, it was found that increasing the contraction ratio leads to a stronger acoustic response in the inertial model. This is primarily due to the lower upstream Mach number and the increased convective acceleration near the nozzle throat, both of which enhance sound generation in the inertial model. The results further revealed that for the inertial model to accurately predict the acoustic response resulting from entropy-patch choked-nozzle interaction, the upstream Mach number must be low. When  $M_u > 0.3$ , a mismatch occurs between the inertial model's predictions and the actual acoustic response. The inertial model tends to underestimate the response, which is likely due to compressible effects that the inertial model does not capture. In contrast, for the matching-condition model, the contraction ratio had a negligible effect on the predictive quality, provided the entropy patch size was sufficiently large relative to the nozzle contraction.

In conclusion, the predictive quality and accuracy of both reduced-order modeling approaches are strongly influenced by specific geometric parameters. For the inertial model, where sound generation relies on the acceleration of an entropy patch through the nozzle, the assumptions of quasi-1D flow and the relative length scale of the patch are critical. In contrast, for the matching-condition (quasi-steady) model, the nozzle shape has little impact as long as the entropy patch is sufficiently large compared to the nozzle.

# Chapter 4

## Conclusions

A comprehensive investigation into the mechanisms governing indirect noise generation due to entropy-patch choked-nozzle interaction was carried out. This was achieved by combining two-dimensional Euler-based numerical simulations with scaling analysis using reduced-order models.

In Chapter 2, the effect of an entropy patch's size, shape, and strength on the upstream acoustic response was investigated using a constant nozzle geometry. The study revealed that the dimensionless streamwise length scale of the entropy patch  $L_s/S_2$  serves as a critical order parameter for determining the dominant sound production mechanism. For patches with  $L_s/S_2 \leq 1$ , one falls in the inertial modeling regime, where the acceleration of an entropy patch through the nozzle is essential for modeling entropy noise. In contrast, for larger entropy patches with  $L_s/S_2 > 1$ , one falls under the matching-condition modeling regime where sound production is dominated by the modulation of thermodynamic state at the nozzle throat.

Two types of entropy patches were considered: circular spots and rectangular (slug-like) blocks. The results indicate that the shape of the entropy patch does have an effect on the predictive accuracy of the reduced-order models. The inertial model provides a better prediction for entropy spots within the inertial modeling regime. While the matching condition provides a better prediction for entropy blocks. However, it should be emphasized that the specific shape of the entropy patch has only a marginal influence on the applicable modeling regime (sound production mechanism).

A major outcome of Chapter 2 is the identification of the entropy-patch strength parameter. The entropy-patch strength  $e'_e/e'_u$  is defined as the ratio of the perturbation area specific energy due to the presence of an entropy patch relative to the total upstream area specific energy. It was found that  $e'_e/e'_u$  acts as an order parameter that can be used to differentiate between linear and non-linear modeling regimes. For weak patches  $e'_e/e'_u \lesssim 1$ , one falls under the linear modeling regime where modeling using linearized models suffices. Beyond this threshold  $e'_e/e'_u > 1$ , nonlinear effects dominate and the predictive accuracy of linearized models diminishes.

In Chapter 3, an investigation of how a nozzle's geometry, particularly the convergent, affects the upstream acoustic response at a constant entropy patch size. Using geometrical parameters of the nozzle convergent, namely the contraction ratio  $C_r = S_1/S_2$ , length ratio  $L_c/S_1$ , and degree  $N$  (determines the inlet's shape).

The results revealed that the predictive accuracy of the reduced-order models is subject to limiting conditions beyond which their performance becomes sensitive to geometric parameters. For the inertial model, it was found that the streamwise length scale of the entropy patch must be small relative to the nozzle convergent length  $L_s/L_c \ll 1$ . In contrast, the matching-condition model's predictive accuracy became independent of the nozzle geometry given that the entropy patch length scale was large relative to the convergent length  $L_s/L_c > 1$ .

Furthermore, by varying the degree of the nozzle's convergent, it was found that the inertial model's predictive accuracy was affected by the degree to which the flow adhered to quasi-1D assumptions. Nozzles with lower values of the quasi-1D parameter  $\max(\frac{S}{R} \frac{dS}{dx})$  showed better agreement with the model predictions, with asymptotic behavior observed for  $\max(\frac{S}{R} \frac{dS}{dx}) \lesssim 1$ . In contrast, the matching-condition model was shown to be largely insensitive to changes in nozzle shape given that  $L_s/S_2 > 1$  &  $L_s/L_c > 1$ . This reaffirms that given a large enough entropy patch, the nozzle effectively acts as a one-dimensional discontinuity.

By changing the contraction ratio of the nozzle, it was revealed that for the inertial model to accurately predict the acoustic response resulting from the entropy-patch choked-nozzle interaction, the upstream Mach number must be low. As runs with a  $M_u > 0.3$  produced an acoustic response which was under-predicted by the inertial model. For the matching-condition model, the contraction ratio had a negligible effect on the predictive validity, provided the entropy patch size was sufficiently large relative to the nozzle contraction.

In conclusion, this thesis makes a significant contribution to the understanding and modeling of indirect noise mechanisms, particularly in indirect entropy noise in choked-nozzle environments. It establishes when and how different modeling strategies apply, equipping researchers and engineers with dimensional parameters for predicting applicable reduced-order models. Moreover, the effect of nozzle geometry on indirect entropy noise modeling strategies allows for nozzle geometries can be optimized not only for flow performance but also for acoustic behavior. These insights are essential for the development of effective noise-mitigation strategies in modern propulsion systems.

# Appendix A

## Supporting derivations

### A.1 Derivation of Reflection coefficient at the nozzle throat

To derive the reflection coefficient at the nozzle throat, consider: the Mach number of the upstream channel

$$M_u = \frac{u_u}{c_u} \quad (\text{A.1})$$

which for a choked-nozzle flow is constant. Thus, taking the total differential one finds:

$$d(M_u) = d\left(\frac{u_u}{c_u}\right) = 0 \quad (\text{A.2})$$

or

$$\frac{c'_u}{c_u} = \frac{u'_u}{u_u} \quad (\text{A.3})$$

This relation can be rewritten as follows:

$$u'_u = c'_u M_u. \quad (\text{A.4})$$

The velocity perturbation  $u'_u$  can be written in terms of left & right traveling waves

$$u'_u = u^+ + u^- = c'_u M_u \quad (\text{A.5})$$

Using d'Alembert's solution to the one-dimensional wave equation & the linearized one-dimensional momentum conservation equation, the velocity waves can be expressed as

$$u^\pm = \pm \frac{p^\pm}{\rho_u c_u} \quad (\text{A.6})$$

This relation is used to rewrite Eq. (A.5), to find

$$\boxed{c'_u = \frac{p^+ - p^-}{M_u \rho_u c_u}}. \quad (\text{A.7})$$

Now consider the isentropic relation ideal gas relation

$$c_u^2 = \gamma \frac{p_u}{\rho_u} \quad (\text{A.8})$$

Taking the total derivative on both sides of this relation, yields

$$2 \frac{c'_u}{c_u} = \frac{p'_u}{p_u} - \frac{\rho'_u}{\rho_u} \quad (\text{A.9})$$

which using the acoustic relation  $\rho'_u = p'_u c_u^{-2}$  can be written as

$$2 \frac{c'_u}{c_u} = \frac{p'_u}{p_u} - \frac{p'_u}{\rho_u c_u^2} = \frac{p'_u}{p_u} \left( 1 - \frac{1}{\gamma} \right) \quad (\text{A.10})$$

Expressing the pressure perturbation in terms of left & right traveling waves and performing some algebra one finds

$$\boxed{c'_u = \frac{c_u(p^+ + p^-)}{2p_u} \left( \frac{\gamma - 1}{\gamma} \right)} \quad (\text{A.11})$$

Noting that Eq. (A.7) and Eq. (A.11) are both expressions for  $c'_u$ : the right-hand side of both equations must equivalent to one another. Thus:

$$\frac{p^+ - p^-}{M_u \rho_u c_u} = \frac{c_u(p^+ + p^-)}{2p_u} \left( \frac{\gamma - 1}{\gamma} \right) \quad (\text{A.12})$$

Now, using Eq. (A.8) one finds

$$(p^+ + p^-) \frac{(\gamma - 1)}{2} = \frac{1}{M_u} (p^+ - p^-) \quad (\text{A.13})$$

The definition of the reflection coefficient is  $R \equiv p^-/p^+$ . Thus, one can perform some algebra to find:

$$R = \frac{1 - \frac{\gamma-1}{2} M_u}{1 + \frac{\gamma-1}{2} M_u} \quad (\text{A.14})$$

## A.2 Derivation of Eq. (2.31)

From the isentropic perfect gas relations, one knows

$$\frac{\rho_u}{\rho_s} = \left( \frac{T_u}{T_s} \right)^{\frac{1}{\gamma-1}} \quad (\text{A.15})$$

Using that  $c = \sqrt{\gamma RT}$  one finds

$$\frac{c_u}{c_s} = \left( \frac{T_u}{T_s} \right)^{\frac{1}{2}}. \quad (\text{A.16})$$

Moreover, one knows

$$T = T_t \left( 1 + \frac{\gamma - 1}{2} M^2 \right)^{-1} \quad (\text{A.17})$$

where the  $t$  subscript indicates total/stagnation conditions. Using the above relation one finds

$$\frac{T_u}{T_s} = \frac{1 + \frac{\gamma-1}{2} M_s^2}{1 + \frac{\gamma-1}{2} M_u^2} \quad (\text{A.18})$$

Using Eq. (A.15), Eq. (A.16) and performing some algebra, one can find:

$$\sqrt{\frac{\rho_u c_u}{\rho_s c_s}} = \left( \frac{T_u}{T_s} \right)^{\frac{\gamma+1}{4(\gamma-1)}} = \left( \frac{1 + \frac{\gamma-1}{2} M_s^2}{1 + \frac{\gamma-1}{2} M_u^2} \right)^{\frac{\gamma+1}{4(\gamma-1)}}$$

which is Eq. (2.31).

### A.3 Derivation of Eq. (2.32)

To find Eq. (2.32): consider that the mass flow rate  $\dot{m}$  at the sound source and the nozzle throat which are equivalent as mass is conserved in the system considered for this study. Assuming the system to be quasi-1-D one has

$$\dot{m} = \rho_s A_s u_s = \rho_{\text{th}} A_{\text{th}} u_{\text{th}} \quad (\text{A.19})$$

N.b., we consider a choked-nozzle flow. Hence, the velocity at the throat is equal to the speed of sound. With that in mind, and using the definition of the Mach number one can write equation above to find:

$$\frac{A_s}{A_{\text{th}}} = \frac{\rho_{\text{th}}}{\rho_s} \frac{1}{M_s} \quad (\text{A.20})$$

Now, using Eq. (A.17), Eq. (A.15), and keeping in mind that one has a sonic condition at the throat one finds

$$A_s = \frac{A_{\text{th}}}{M_s} \left( 1 + \frac{\gamma - 1}{\gamma + 1} (M_s^2 - 1) \right)^{\frac{\gamma+1}{2(\gamma-1)}}$$

which is Eq. (2.32).

### A.4 A relation for the acoustic power emitted from the sound source

A general expression for the emitted acoustic power  $\Phi$  through a surface of area  $A$  is

$$\Phi = I A \quad (\text{A.21})$$

where  $I$  is the acoustic intensity. Howe [44] showed that the acoustic intensity of an irrotational homentropic (quasi-steady-1D) flow is

$$I = (\bar{\rho}u' + \rho'\bar{u})B' \quad (\text{A.22})$$

where the bar indicates mean-flow quantities and the prime perturbations.  $B'$  is the total enthalpy fluctuation which can be expressed in terms of pressure perturbation  $p'$ ,  $\bar{\rho}$ ,  $\bar{u}$ , and  $u'$ , as follows:

$$B' = \frac{p'}{\bar{\rho}} + \bar{u}u'. \quad (\text{A.23})$$

Using the relation  $u^\pm = \pm(p^\pm/\bar{\rho}\bar{c})$  and only considering upstream-traveling waves the total enthalpy fluctuations can be written as

$$B^- = \frac{p^-}{\bar{\rho}} - \frac{p^-\bar{u}}{\bar{\rho}\bar{c}} = \frac{p^-}{\bar{\rho}}(1 - M) \quad (\text{A.24})$$

where  $M$  is the unperturbed flow Mach number. Using Eq. (A.24) and rewriting the velocity and density perturbations the acoustic intensity of upstream traveling acoustic wave can be expressed as

$$I^- = \left( \frac{-p^-}{\bar{c}} + \frac{p^-\bar{u}}{\bar{c}^2} \right) \frac{p^-}{\bar{\rho}}(1 - M) = -\frac{(p^-)^2}{\bar{\rho}\bar{c}}(1 - M)^2. \quad (\text{A.25})$$

this allows one to express the acoustic power of an upstream traveling acoustic wave as follows

$$\Phi^- = -\frac{A(p^-)^2}{\bar{\rho}\bar{c}}(1 - M)^2. \quad (\text{A.26})$$

## A.5 Establishing choked-nozzle flow

Establishing a choked-nozzle flow is done by imposing an upstream inflow velocity  $U_{\text{des}}$ . This is desired velocity is determined by using the quasi-1-D relation for steady critical throat mass-flow rate [42]:

$$\dot{m}_{\text{th}}^* = \rho_{\text{th}}U_{\text{th}}A_{\text{th}} = \left( \frac{2}{\gamma + 1} \right)^{\frac{\gamma+1}{2(\gamma-1)}} \rho_u c_u A_{\text{th}} \quad (\text{A.27})$$

where  $\dot{m}^*$  is the critical throat mass flow rate,  $\rho$  is the density,  $U$  is the velocity,  $A$  is the area,  $c$  is the speed of sound, and  $\gamma$  is the specific heat ratio. The subscripts indicate the location; viz.,  $th$  for the throat and  $u$  for the upstream channel.

We note that the mass-flow rate at the inlet of the nozzle is equal to the mass flow at the throat. I.e., we have

$$\rho_u U_u A_u = \rho_{\text{th}} U_{\text{th}} A_{\text{th}} \quad (\text{A.28})$$

Using the relation above one rewrites Eq. (A.27) to find

$$U_u = \left( \frac{2}{\gamma + 1} \right)^{\frac{\gamma+1}{2(\gamma-1)}} c_u \frac{A_{\text{th}}}{A_u} \quad (\text{A.29})$$

which is used to specify  $U_{\text{des}}$ .

## A.6 Derivation of Eq. (2.41)

We define the strength of an entropy patch as follows:

$$\frac{e'_e}{e_u} \equiv \frac{e_e - e_u}{e_u}. \quad (\text{A.30})$$

If we consider the general definition of area-specific energy

$$e = \rho \left( c_v T + \frac{1}{2} u^2 \right) \quad (\text{A.31})$$

and use the ideal-gas law to rewrite  $\rho T$  term, one finds:

$$e = p \left( \frac{c_v}{R} \right) + \frac{1}{2} \rho u^2. \quad (\text{A.32})$$

Using this relation to rewrite the energy terms in the numerator of Eq. (A.30), yields

$$\frac{e'_{\text{patch}}}{e_u} = \frac{\frac{c_v}{R}(p_e - p_u) + (\frac{1}{2}\rho_e u_e^2 - \frac{1}{2}\rho_u u_u^2)}{\rho_u(c_v T_u + \frac{1}{2}u_u^2)} \quad (\text{A.33})$$

Noting that  $p_e = p_u$  for mature entropy patches and that the entropy patch is convected by the flow ( $u_e = u_u$ ), this expression can be rewritten to find:

$$\frac{e'_e}{e_u} = \frac{\rho_e - \rho_u}{\rho_u} \frac{\frac{1}{2}u_u^2}{c_v T_u + \frac{1}{2}u_u^2} = \frac{\rho'_e}{\rho_u} \left[ \frac{u_u^2}{2c_v T_u} + 1 \right]. \quad (\text{A.34})$$

Now, using the definition of the Mach number  $M = u/c$ , speed of sound of ideal gases  $c = \sqrt{\gamma R T}$ , specific heat ratio  $\gamma = c_p/c_v$ , and  $R = c_p - c_v$ , we, after some algebra, find

$$\frac{e'_e}{e_u} = \frac{\rho'_e}{\rho_u} \left[ \frac{2}{\gamma(\gamma - 1)M_u^2} + 1 \right]$$

which is Eq. (2.41).

## A.7 Generating entropy patches with similar relative excess density or excess mass

As one aims to produce entropy patches with similar relative excess density or excess mass, one must be able to estimate the change in density due to energy injection in the system. This can be done by considering the total energy density of a system  $E$ , which for a perfect gas is given by

$$E = \frac{p}{\rho(\gamma - 1)} + \frac{1}{2} |\mathbf{U}|^2 \quad (\text{A.35})$$

where  $p$ ,  $\rho$ ,  $\mathbf{U}$ , and  $\gamma$  are the pressure, density, velocity vector, and specific heat ratio. Assuming the pressure and velocity of our system are the same before and

after the generation of the entropy patch one can estimate the density of the system after energy injection to be<sup>1</sup>.

$$\rho_2 = \frac{p\rho_1}{\Delta E\rho_1(\gamma - 1) + p} \quad (\text{A.36})$$

$\rho_1$  and  $\rho_2$  indicate the density before and after the entropy patch generation. The relative excess density can be found as follows:

$$\frac{\rho'_e}{\rho_u} = \frac{\rho_2 - \rho_1}{\rho_1} = \frac{p}{\Delta E\rho_1(\gamma - 1) + p} - 1 \quad (\text{A.37})$$

Similarly, the excess mass can be as follows

$$m_e = A_e(\rho_2 - \rho_1) = -A_e \frac{\Delta E\rho_1^2(\gamma - 1)}{\Delta E\rho_1(\gamma - 1) + p} \quad (\text{A.38})$$

where  $A_e$  is the area of the entropy patch. The change of the energy of the system  $\Delta E$  is equal to the total energy produced by the source term  $Q_E$  (Eq. (2.37)) used to generate entropy patches. To find the total energy produced by the source term  $Q_E$  one has to take its integral with respect to space and time

$$\Delta E = \iint Q_E(\zeta, t) dA dt. \quad (\text{A.39})$$

The steps taken to come up with the entropy generation settings are as follows. Firstly, the total generation time scale ( $\tau_{\text{total}} = \tau_{\text{start}} + \tau_{\text{max}} + \tau_{\text{end}}$ ) is determined as it is bound by the length of the generation block  $L_{B3}$ , streamwise length scale of the entropy patch  $L_s$  and the velocity of the upstream base flow  $u_u$ .

$$\tau_{\text{total}} = \frac{L_{B3} - 2L_s}{u_u} \quad (\text{A.40})$$

After  $\tau_{\text{total}}$  is determined the required values of  $A_{\text{max}}$ ,  $\tau_{\text{start}}$ ,  $\tau_{\text{max}}$ , and  $\tau_{\text{end}}$  used to achieve a specific relative excess density or excess mass are found using Equations (A.37) to (A.39). The values of  $\rho_1$  and  $p$  used to find the required entropy generation settings are obtained from the flow field resulting from the intermediate run.

---

<sup>1</sup>It should be noted that finding the density of the system after energy injection is a non-trivial task as the entropy patch generation process is not isentropic, isothermal, or isobaric.

# Appendix B

## Supporting studies

### B.1 Pressure Signal Error Quantification

When performing numerical simulations, it is inevitable that errors arise due to modeling assumptions, discretization schemes, solver algorithms, boundary & initial conditions, & machine precision [45]. Hence, to establish confidence in simulation results, it is crucial to quantify the numerical error.

To quantitatively determine the numerical error for the ECNI runs, the Richardson extrapolation method was applied [45]. The Richardson extrapolation makes use of two solutions  $f_1$  &  $f_2$ , each obtained with a different grid spacing value, to approximate the exact solution  $f_e$  of the quantity of interest as follows:

$$f_e = f_1 + \frac{f_1 - f_2}{r^{p_e} - 1}; \quad r = \frac{h_2}{h_1}; \quad h_2 > h_1 \quad (\text{B.1})$$

where  $h_1$  &  $h_2$  are the grid spacing used for  $f_1$  &  $f_2$ , respectively.  $p_e$  is the expected order of accuracy of the numerical scheme used.

However, Eq. (B.1) only holds true if meshes with spacing  $h_1$  &  $h_2$  are within the asymptotic region of the discretization. This can be checked by computing the observed order of accuracy  $p_o$ . To do this, one introduces a third solution  $f_3$  at a grid spacing  $h_3$ , where  $h_3 = rh_2$ .

$$p_o = \frac{\ln\left(\frac{f_3 - f_2}{f_2 - f_1}\right)}{\ln(r)} \quad (\text{B.2})$$

If  $p_o$  is sufficiently close to  $p_e$ , one has a good indication that  $f_1$ ,  $f_2$  &  $f_3$  lie on the asymptotic region of convergence.

With that, three meshes with varying grid spacing were made using a refinement ratio of  $r = 1.5$ . Where the coarsest mesh has a base value of 100 points per meter (PPM), the intermediate mesh has a base value of 150 PPM, while the finest mesh has a base value of 225 PPM. The quantity of interest  $f$  used to establish convergence was the maximum amplitude of the pressure perturbation  $p'$  due to an upstream traveling acoustic wave at a probe location in the 1-D extraction domain. The pressure perturbation was defined as follows:  $p' \equiv p - p_{\text{ref}}$  where  $p$  is the full pressure signal &  $p_{\text{ref}}$  is the average pressure after the transient flow features have passed.

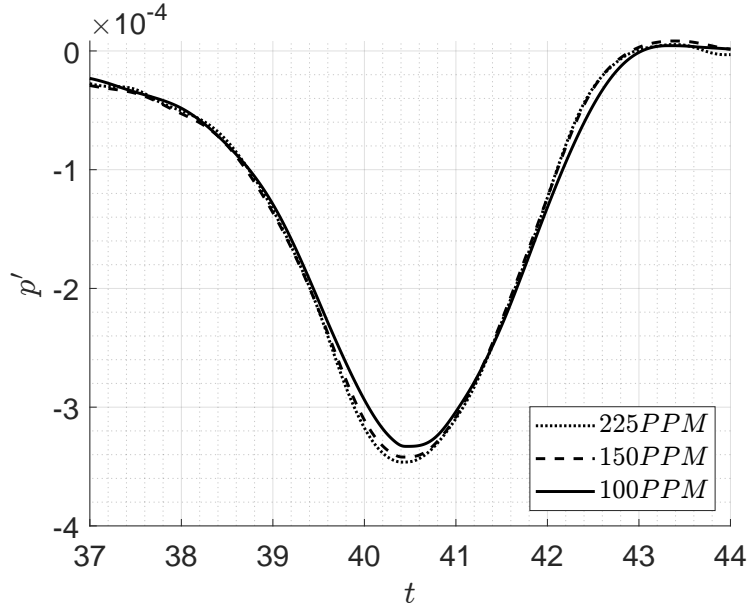


FIGURE B.1: Measured upstream perturbation pressure signal at varying grid refinement levels.

ECNI runs were made using Elbakly’s computational procedure [33]. A spot radius of  $R_s = 0.2$  m was used for said ENCI runs. The resulting upstream acoustic responses (Fig. B.1) were then used to carry out a Richardson extrapolation analysis.

Given that a (5,2) Runge-Kutta scheme was used for the time discretization & a Roe-TVD scheme with a Van Leer limiter for the spatial discretization, one expects the accuracy of the system to be of order two.

Elbakly determined that an observed order of accuracy  $p_o = 1.9$  in his results. This is judged sufficiently close to the expected order of accuracy to assume that one is in the asymptotic region of grid convergence.

With that in mind, the numerical error was quantified, and the results are shown in Table B.1. To generalize the findings such that they can be used as a starting point for grid production, the error is also reported in points per wavelength (PPW) of the upstream traveling acoustic wave, as well as points per radius (PPR) of the entropy spot.

As the PPW values are much greater than the required base 50 PPW reported by Hulshoff [32] to maintain an acoustic wave with sufficient accuracy, the PPR was used as a base design guideline. Where a PPR = 30 was used as it has a good computational time to error ratio, given the machine that was used to run the computations.

PPM	PPW	PPR	Error (%)
100	407	20	4.88
150	611	30	2.20
225	917	45	0.98

TABLE B.1: Discretization error of upstream pressure perturbation due to entropy patch choked-nozzle interaction at different grid refinement levels.

# References

- [1] T. Abdallah, “Chapter 6 - environmental impacts of mass transit operations,” in *Sustainable Mass Transit (Second Edition)* (T. Abdallah, ed.), pp. 77–93, Elsevier, second edition ed., 2023.
- [2] “Paris agreement.” United Nations Treaty Collection, Chapter XXVII 7. d.
- [3] J. Beita, M. Talibi, S. Sadasivuni, and R. Balachandran, “Thermoacoustic instability considerations for high hydrogen combustion in lean premixed gas turbine combustors: A review,” *Hydrogen*, vol. 2, pp. 33–57, Jan. 2021.
- [4] J. J. Keller, “Thermoacoustic oscillations in combustion chambers of gas turbines,” *AIAA J.*, vol. 33, pp. 2280–2287, Dec. 1995.
- [5] S. Candel, “Combustion dynamics and control: Progress and challenges,” *Proc. Combust. Inst.*, vol. 29, pp. 1–28, Jan. 2002.
- [6] A. P. Dowling and S. R. Stow, “Acoustic analysis of gas turbine combustors,” *J. Propuls. Power*, vol. 19, pp. 751–764, Sept. 2003.
- [7] A. P. Dowling and Y. Mahmoudi, “Combustion noise,” *Proceedings of the Combustion Institute*, vol. 35, no. 1, pp. 65–100, 2015.
- [8] A. S. Morgans and I. Duran, “Entropy noise: A review of theory, progress and challenges,” *International Journal of Spray and Combustion Dynamics*, vol. 8, no. 4, pp. 285–298, 2016.
- [9] T. C. Lieuwen, *Unsteady Combustor Physics*. Cambridge University Press, Aug. 2012.
- [10] A. C. Benim and K. J. Syed, *Flashback mechanisms in lean premixed gas turbine combustion*. Academic press, 2014.
- [11] J. B. Sewell and P. A. Sobieski, “Monitoring of combustion instabilities: Calpine’s experience,” *Progress in astronautics and aeronautics*, vol. 210, p. 147, 2005.
- [12] W. C. Strahle, “On combustion generated noise,” *Journal of Fluid Mechanics*, vol. 49, no. 2, pp. 399–414, 1971.
- [13] A. Genot, “Aluminum combustion instabilities: Dimensionless numbers controlling the instability in solid rocket motors,” *Combustion and Flame*, vol. 232, p. 111563, 2021.

- [14] L. Hirschberg, F. Bake, K. Knobloch, S. Hulshoff, and A. Hirschberg, “Experimental investigations of indirect noise due to modulation of axial vorticity and entropy upstream of a choked nozzle,” *Journal of sound and vibration*, vol. 532, 2022.
- [15] I. Duran and S. Moreau, “Solution of the quasi-one-dimensional linearized euler equations using flow invariants and the magnus expansion,” *Journal of Fluid Mechanics*, vol. 723, p. 190–231, 2013.
- [16] M. Leyko, F. Nicoud, and T. Poinsot, “Comparison of direct and indirect combustion noise mechanisms in a model combustor,” *AIAA Journal*, vol. 47, p. 2709–2716, Nov. 2009.
- [17] J. Anthoine, J.-M. Buchlin, and A. Hirschberg, “Effect of nozzle cavity on resonance in large srm: Theoretical modeling,” *Journal of Propulsion and Power*, vol. 18, no. 2, pp. 304–311, 2002.
- [18] F. Bake, C. Richter, B. Muhlbauer, N. Kings, I. Rohle, F. Thiele, and B. Noll, “The entropy-wave generator (EWG): A reference case on entropy noise,” *Journal of Sound and Vibration*, pp. 574–598, 2009.
- [19] N. Kings and F. Bake, “Indirect combustion noise: noise generation by accelerated vorticity in a nozzle flow,” *International Journal of Spray and Combustion Dynamics*, vol. 2, no. 3, pp. 253–266, 2010.
- [20] N. Kings, *Indirect combustion noise: Experimental investigation of the vortex sound generation in nozzle flows*. PhD thesis, Technische Universität Berlin, 2015.
- [21] L. Hirschberg, F. Bake, K. Knobloch, and S. J. Hulshoff, “Swirl-nozzle interaction experiments: Influence of injection-reservoir pressure and injection time,” *AIAA Journal*, vol. 59, no. 7, pp. 2806–2810, 2021.
- [22] F. De Domenico, E. Rolland, J. Rodrigues, L. Magri, and S. Hochgreb, “Compositional and entropy indirect noise generated in subsonic non-isentropic nozzles,” *Journal of Fluid Mechanics*, vol. 910, pp. A5 1–31, 2021.
- [23] M. Wellemann and N. Noiray, “Experiments on sound reflection and production by choked nozzle flows subject to acoustic and entropy waves,” *Journal of Sound and Vibration*, vol. 492, p. 115799, 2021.
- [24] L. Hirschberg, F. Bake, K. Knobloch, A. Rudolphi, S. Kruck, O. Klose, and S. J. Hulshoff, “Swirl-nozzle interaction experiment: Quasi-steady model based analysis,” *Experiments in Fluids*, vol. 62, no. 175, pp. 1–16, 2021.
- [25] F. E. Marble and S. M. Candel, “Acoustic disturbance from gas non-uniformities convected through a nozzle,” *Journal of Sound and Vibration*, vol. 55, pp. 225–243, 1977.

- [26] J. E. Ffowcs Williams and M. S. Howe, “The generation of sound by density inhomogeneities in low mach number nozzle flows,” *Journal of Fluid Mechanics*, vol. 70, no. 3, pp. 605–622, 1975.
- [27] M. Leyko, S. Moreau, F. Nicoud, and T. Poinso, “Numerical and analytical modeling of entropy noise in a supersonic nozzle with a shock,” *Journal of Sound and Vibration*, vol. 330, no. 16, pp. 3944–3958, 2011.
- [28] L. Hirschberg and S. J. Hulshoff, “Lumped-element model for vortex-nozzle interaction in solid rocket motors,” *AIAA Journal*, vol. 58, no. 7, pp. 3241–3244, 2020.
- [29] Y. Gentil, G. Daviller, S. Moreau, and T. Poinso, “Multispecies flow indirect-noise modeling re-examined with a helicopter-engine application,” *AIAA Journal*, pp. 1–14, 2024.
- [30] K. Kowalski, S. J. Hulshoff, P. Ströer, J. Withag, A. Genot, A. S. Morgans, F. Bake, K. Venner, M. Sanders, and L. Hirschberg, “Entropy-patch-choked-nozzle interaction: Quasi-steady-modeling-regime limits probed,” in *30th AIAA/CEAS Aeroacoustics Conference (2024)*, vol. 2009, American Institute of Aeronautics and Astronautics, May 2024.
- [31] K. Kowalski, “Entropy-patch choked-nozzle interaction: matching-condition and inertial-effects regimes mapped & preliminary investigations of amplitude effects,” Master’s thesis, University of Twente, 2024.
- [32] S. J. Hulshoff, *EIA an Euler Code for Internal Aeroacoustics: method description and user’s guide*. Faculty of Aerospace Engineering, Delft University of Technology, Delft, the Netherlands, October 2016.
- [33] K. Elbakly, “Euler computations of internal aeroacoustics: Development and application of numerical solution techniques for indirect combustion noise,” tech. rep., TU Delft, 2024.
- [34] L. Hirschberg, *Low order modeling of vortex driven self-sustained pressure pulsations in solid rocket motors*. Theses, Université Paris Saclay (COMUE), Jan. 2019.
- [35] P. Thompson, *Compressible-fluid Dynamics*. Advanced engineering series, McGraw-Hill, 1972.
- [36] N. Curle, “The influence of solid boundaries upon aerodynamic sound,” *Proc. Roy. Soc. A*, vol. 231, pp. 505–514, 1955.
- [37] A. D. Pierce, *Acoustics: an introduction to its physical principles and applications*. Melville, New York, USA: Acoustical Society of America, 1994.
- [38] S. J. Hulshoff, A. Hirschberg, and G. C. J. Hofmans, “Sound production of vortex nozzle interactions,” *Journal of Fluid Mechanics*, vol. 439, pp. 335–352, July 2001.

- [39] L. Hirschberg, S. J. Hulshoff, J. Collinet, C. Schram, and T. Schuller, “Vortex nozzle interaction in solid rocket motors: A scaling law for upstream acoustic response,” *Journal of the Acoustical Society of America*, vol. 144, no. 1, pp. EL46–EL51, 2018.
- [40] L. Hirschberg, S. J. Hulshoff, J. Collinet, C. Schram, and T. Schuller, “Influence of nozzle cavity on indirect vortex- and entropy-sound production,” *AIAA Journal*, vol. 57, no. 7, pp. 3100–3103, 2019.
- [41] P. Henrici, *Applied and Computational Complex Analysis*, vol. I. NY, USA: Wiley-Interscience, 1974.
- [42] M. E. H. van Dongen, A. Hirschberg, and D. M. J. Smeulders, *Fundamentals of gas dynamics*, 2023.
- [43] L. Crocco, *B. One-Dimensional Treatment of Steady Gas Dynamics*, pp. 64–349. Princeton: Princeton University Press, 1958.
- [44] M. S. Howe, *Acoustics of Fluid-Structure Interactions*, p. 81. Cambridge Monographs on Mechanics, Cambridge University Press, 1998.
- [45] S. J. Hulshoff, *Computational Modelling*. Faculty of Aerospace Engineering, Delft University of Technology, Delft, the Netherlands, 2021.